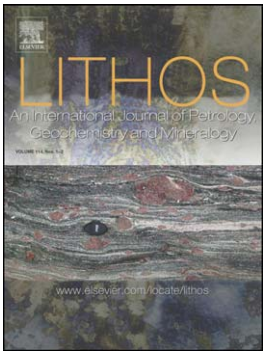

Multiple sources of the Early Mesozoic Gouli batholith, Eastern Kunlun Orogenic Belt, northern Tibetan Plateau: linking continental crustal growth with oceanic subduction

Jiajie Chen, Junhao Wei, Lebing Fu, Huan Li, Hongzhi Zhou, Xu Zhao, Xiaofei Zhan, Jun Tan

PII: S0024-4937(17)30307-9
DOI: doi:10.1016/j.lithos.2017.09.006
Reference: LITHOS 4412

To appear in: *LITHOS*

Received date: 9 June 2017
Accepted date: 3 September 2017

Please cite this article as: Chen, Jiajie, Wei, Junhao, Fu, Lebing, Li, Huan, Zhou, Hongzhi, Zhao, Xu, Zhan, Xiaofei, Tan, Jun, Multiple sources of the Early Mesozoic Gouli batholith, Eastern Kunlun Orogenic Belt, northern Tibetan Plateau: linking continental crustal growth with oceanic subduction, *LITHOS* (2017), doi:10.1016/j.lithos.2017.09.006

Multiple sources of the Early Mesozoic Gouli batholith, Eastern Kunlun Orogenic Belt, northern Tibetan Plateau: linking continental crustal growth with oceanic subduction

Jiajie Chen[1,2], Junhao Wei[1], Lebing Fu[1], Huan Li[1], Hongzhi Zhou[1], Xu Zhao[1], Xiaofei Zhan[1], Jun Tan[1]

1. Faculty of Earth Resources, China University of Geosciences, Wuhan 430074, China

2. Department of Earth Sciences, University of Durham, Durham, DH1 3LE, UK

Corresponding author

Lebing Fu

Faculty of Earth Resources, China University of Geosciences,

Lumo Road No. 388, Hongshan District, Wuhan 430074,

Hubei Province, China.

E-mail: fulb@cug.edu.cn, fulebing1212@126.com

Tel: +86-13429802569, Fax: +86-27-67883053.

Abstract: Orogenic belts have been among the most important locations to investigate the growth of continental crust (CC). The Eastern Kunlun Orogenic Belt (EKOB), which contains widespread Permian–Triassic granitoids, is volumetrically comparable to the Cenozoic Gangdese magmatic belt in the Tibetan Plateau and is an ideal region to investigate the mechanism of the Paleozoic–Mesozoic CC growth in this region. The Gouli batholith at the eastern end of the EKOB consists of the synchronous Xiangride granodiorite, Asiha quartz diorite (ca. 242 Ma) and adamellite. The granodiorite and quartz diorite, both of which contain magmatic enclaves, show medium–high K, calc-alkalic and metaluminous signatures and have similar rare earth element and trace element patterns to those of bulk CC. Besides, the Xiangride granodiorite displays distinct adakitic signatures (average Sr/Y of 47). The Sr-Nd isotopic values for the different types of rocks are roughly similar ($(^{87}Sr/^{86}Sr)_i$ = 0.708167–0.713553, $\varepsilon_{Nd}(t)$ = -6.8 to -5.3), while Hf isotopes are distinguishable, with $\varepsilon_{Hf}(t)^{granodiorite}$ = 0.3 to 5.1 and $\varepsilon_{Hf}(t)^{diorite}$ = -1.6 to 0.7. These geochemical and petrographic signatures suggest that the granodiorite originated from the partial melting of subducting oceanic crust and terrigenous sediments, and the quartz diorite and enclaves formed via the mixing of slab-derived magma and enriched mantle-derived melt. Further comprehensive analyses of the spatial and temporal distribution of regional magmatic rocks, metamorphism and sedimentary facies reveal that the Gouli batholith and most of the Permian–Triassic granitoids in the EKOB formed during the subduction of the Paleo-Tethys Ocean instead of subsequent syn-collision setting. Thus, we contend that the Permian–Triassic CC growth of the EKOB occurred in a slab

subduction setting and that both oceanic slab and subcontinental mantle significantly contributed to this process.

Keywords:

Middle Triassic; Mafic microgranular enclaves; Magma mixing; Continental crustal growth; Paleo-Tethys; Eastern Kunlun Orogenic Belt.

1. Introduction

The origin and evolution of continental crust (CC) is a debated topic in the geosciences. The andesitic composition and arc-like chemical signatures of bulk CC (enriched in large ion lithophile elements (LILEs) and depleted in high field strength elements (HFSEs)) have led to the predominant “island arc” model (Taylor, 1967; 1977), which emphasizes that magma that is produced during slab subduction contributes to its growth. However, a recently proposed alternative hypothesis (“continental collision” model) suggests that net CC growth occurs during continental collision rather than slab subduction (Mo et al., 2008; Niu and O'Hara, 2009; Niu et al., 2013). This new hypothesis has been applied to the Gangdese belt (Mo et al., 2008; Niu et al., 2013), Eastern Kunlun Orogenic Belt (EKOB; Huang et al., 2014; Shao et al., 2017) and Qilian Orogen (Zhao et al., 2017). The main differences involve the materials that contribute to CC growth and the tectonic background in which the CC growth occurs. The former model emphasizes that materials from the upper mantle build the CC in a subduction setting (Taylor, 1967; Shirey and Hanson, 1984), while the latter model contends that the CC-building materials are derived from oceanic crust under a continental-collision background (Mo et al., 2008; Niu and O'Hara, 2009; Niu et al., 2013). Obviously, a detailed investigation of the rock-forming tectonic setting and origin of CC-building rocks (granitoid/andesite) jointly should shed some light on the mechanism of CC growth. The EKOB, one of the belts to which “continental collision” model has been applied (Huang et al., 2014; Shao et al., 2017), should be an ideal location to discuss this issue for the following

reasons: (1) granitoids with similar average geochemical signatures to CC are widespread in this belt (e.g., Huang et al., 2014; Xiong et al., 2014); (2) the EKOB contains continental collision-related rocks and inherited mass subduction-related magmatic rocks that formed in an earlier stage (e.g., Xia et al., 2015); and (3) the "continental collision" model has been discussed in detail regarding the crustal growth of the EKOB (Huang et al., 2014; Shao et al., 2017), providing a chance to compare the two models. Although, mechanism of CC growth in different orogenic belts may vary, our study should still shed some light on the general mechanism of CC growth.

The EKOB, which is located in the northern Tibetan Plateau and bounded to the north by the Qaidam Basin, is a giant tectono-magmatic belt that is similar to the Gangdese magmatic belt (Fig. 1; Mo et al., 2007). The EKOB recorded two stages of orogenesis, i.e., Late Neoproterozoic–Early Paleozoic Proto-Tethys-related and Late Paleozoic–Mesozoic Paleo-Tethys-related orogenesis (Mattern et al., 1996; Yang et al., 1996; Chen et al., 2001; Mo et al., 2007; Liu et al., 2011). Large amounts of granitoids were generated during these orogenic events (Mo et al., 2007) and Permian-Triassic granitoids with abundant mafic magmatic enclaves (MMEs) predominate in the EKOB (Liu et al., 2002; Xiong, 2014; Ma et al., 2015). These rocks show metaluminous and medium–high-K calc-alkaline signatures, similar to those of the average CC, and thus offer an ideal opportunity to investigate the mechanism of CC growth. Recent research on the granitoids in the EKOB proposed that these Permian–Triassic granitoids formed during continental collision, which was used as evidence of net CC growth in the collision zone (Huang et al., 2014; Shao et al., 2017).

However, the rock-forming setting, the cornerstone of the above conclusion, remains under debate. The timings of the ocean closure and subsequent continent-continent collision are still ambiguous. Huang et al. (2014) argued that the A'nyemaqen Ocean (a portion of Paleo-Tethys Ocean) closed at the beginning of the Late Permian according to the Late-Permian molasse deposits and the angular unconformity between the Upper-Permian and Lower-Permian strata in the EKOB (Fig. 2). Xiong et al. (2014) proposed that the initial collision between the Bayan Har Terrain (BHT) and southern Eastern Kunlun Terrain (SEKT) occurred at 231 Ma based on an investigation of granitoids and their enclaves. Xia et al. (2015b) suggested that the ocean closed at 243 Ma according to a newly recognized micro-angular unconformity between the Middle Triassic Xilikete and Naocangjiangou Formations (Fig. 2). In addition, other researchers contended that the subduction of the A'nyemaqen Ocean continued until the Late Triassic (Roger et al., 2003; Gehrels et al., 2011). This indeterminacy of the tectonic evolution obstructs the understanding of the rock-forming tectonic setting, the petrogenesis of the widespread Permian–Triassic granitoids, and, thus, the understanding of the mechanism of CC growth in the EKOB. Thus, a detailed discussion on the tectonic evolution and petrogenesis of the Permian–Triassic granitoids based on the tectonic setting is the key to reveal the detailed mechanism of CC growth in the EKOB.

The Triassic Gouli batholith, which is situated at the eastern end of the EKOB, displays clear CC-like geochemical signatures. Thus, a comprehensive study of this batholith should provide insight into the detailed mechanism of CC growth in this area. In this paper, we

present new zircon U-Pb dating results and geochemical and Sr-Nd-Hf isotopic data for the Gouli batholith to: (1) discuss the tectonic setting of the widespread Permian-Triassic magmatism, (2) investigate the origin and petrogenesis of the Gouli batholith, and (3) constrain the mechanism of CC growth in the EKOB.

2. Geological setting

The EKOB, which is separated by the central Eastern Kunlun Suture zone (CEKS) and southern Eastern Kunlun Suture zone (SEKS), consists of the northern Eastern Kunlun Terrane (NEKT), SEKT and BHT from north to south. The basement rocks that are exposed in the NEKT and SEKT include high-grade metamorphic rocks from the Paleoproterozoic Jinshuikou Group (Wang et al., 2007; He et al., 2016), which are covered by Paleozoic sedimentary and low-grade metamorphic rocks. Mesozoic and Cenozoic sedimentary and volcanic rocks mainly occur in the SEKT and BHT. Investigations on the sedimentary facies indicated that the Carboniferous–Middle Triassic strata are marine facies, while the Upper Triassic Babaoshan Formation is lake or river facies (R.B. Li et al., 2012 and unpublished report). Regionally, four unconformities have been recognized from the Carboniferous–Triassic strata in the EKOB. From bottom to top, these features are an angular unconformity between the Upper Permian Gequ Formation and Upper Carboniferous Haoteluowa Formation, a micro-angular unconformity between the Middle Triassic Xilikete Formation and Naocangjiangou Formation, an angular unconformity between the Upper Triassic Babaoshan Formation and underlying strata, and an angular unconformity between the Lower Jurassic Yangqu

Formation and Upper Triassic Babaoshan Formation (Fig. 2; R.B. Li et al., 2012 and unpublished report).

Early Paleozoic-Mesozoic Magmatic rocks prevail in the EKOB with two episodes during 470–390 Ma and 260–220 Ma (Mo et al., 2007; Li, 2012). The latter are mainly exposed in the NEKT (Fig. 1B), with time-varying lithology from early granodiorite and tonalite (Late Permian-Middle Triassic; Liu, 2008; Chen et al., 2011; Xiong, 2014) to late alkali granite (Late Triassic; Li et al., 2008; Zhang, 2012; Gao, 2013). MMEs are common in the granodiorite, and most of them are coeval with the host rocks, such as the Bairiqili intrusion (248 Ma for the host granodiorite and 250 Ma for enclaves; Xiong, 2014) and Yuegelu intrusion (242 Ma for the host rocks and 241 Ma for enclaves; Liu et al., 2004).

The Gouli study area is situated at the eastern end of the EKOB (Fig. 1B). The principal strata that were intruded by Mesozoic granitoids (Gouli batholith) are Proterozoic metamorphic rocks, which consist of paragneiss, orthogneiss, amphibolite, marble and migmatite (He et al., 2016), and the Ordovician Naij Tai Group, which consists of low-grade meta-volcanic and meta-sedimentary rocks (Chen et al., 2014). Magmatic rocks are widespread and predominantly include granodiorite (Xiangride intrusion), adamellite and quartz diorite (Asiha intrusion) with minor hornblende gabbro (Annage intrusion; Fig. 1C). These rocks (excluding the hornblende gabbro) compose the Gouli batholith, which covers more than 200 km^2 (unpublished report). Previous studies revealed that the emplacement of the adamellite, quartz diorite and hornblende gabbro occurred at 237–242 Ma (Xiong, 2014), 238–244 Ma (B.Y. Li et al., 2012; J.C. Li et al., 2014) and 242±2 Ma (Zhao et al., in

press), respectively, coeval with the Xialamusong batholith to the north (Mo et al., 2007; Ma et al., 2015). The major and trace element compositions of the quartz diorite were also reported, indicating medium- to high-K and metaluminous attributes and a subduction-related origin of this rock (B.Y. Li et al., 2012; J.C. Li et al., 2014).

3. Petrography and sampling

3.1. Xiangride granodiorite and its enclaves

The Xiangride granodiorite, which is located in the northwestern section of the study area, comprises the majority of the Gouli batholith (Fig. 1C) and hosts sparse enclaves (Fig. 3A–C). The granodiorite is medium–coarse grained and consists of amphibole (2 %), biotite (5 %), plagioclase (40–50 %), K–feldspar (10–20 %), quartz (20–30 %), with minor accessory titanite and zircon. Plagioclase crystals are euhedral–subhedral and frequently show distinct zoning texture (Fig. 3D). Amphibole, biotite and K-feldspar are euhedral–subhedral, while quartz is irregularly-grained (Fig. 3D–F).

Enclaves that are small (3–13 cm) and scattered in the granodiorite have sharp contacts with the host rocks (Fig. 3B and C) and exhibit oval-linear shapes. These enclaves consist of amphibole (30–40 %), biotite (5 %), feldspar (45–55 %), quartz (5 %), apatite (3 %), and minor titanite and zircon (Fig. 3E–I). Quartz and plagioclase phenocrysts occur as medium–coarse grains or elongated laths in the groundmass, with the latter showing distinct growth zonings (Fig. 3C and G–H). The distinct resorption textures of the medium–coarse plagioclase grains indicate that these larger crystals (Fig. 3C and H) did not

directly crystallize from the enclave-forming magma, but were captured from another source. The groundmass mainly consists of fine-grained quartz, feldspar, amphibole, and euhedral biotite. The minor apatite is acicular and entrapped in feldspar (Fig. 3I).

3.2. Asiha quartz diorite

The Asiha quartz diorite, which includes abundant MMEs, occurs in the eastern section of the study area (Figs. 1C and 3J). This diorite shows medium–coarse grained, equigranular texture and mainly comprises amphibole (5–10 %), biotite (5–7 %), plagioclase (60–70 %), K-feldspar (10–20 %) and quartz (10–15 %), with minor apatite, zircon and opaque minerals (Fig. 3K–L). The amphiboles are euhedral–subhedral with occasional feldspar inclusions (Fig. 3K). The biotite crystals are subhedral and sometimes enwrapped in feldspars or amphiboles. The plagioclase shows long column shapes with occasional growth zonings. The anhedral quartz is intergrown with feldspar grains (Fig. 3K–L). The enclaves within the quartz diorite are rounded, ellipsoidal, elongated without solid-state deformation (Fig. 3J), and much larger in size (3–70 cm) and more intensive than those that are enclosed in the granodiorite. These enclaves mainly comprise hornblende, feldspar, quartz, biotite and acicular apatite (B.Y. Li et al., 2012).

The sample locations for the Xiangride granodiorite and its enclaves and those for the Asiha quartz diorite are illustrated in Fig. 1C.

4. Analytical methods

4.1. Zircon U–Pb dating and trace element determination

Zircon grains were separated from the samples by conventional magnetic and density techniques at the laboratory of the Langfang Regional Geological Survey Institute in the Hebei Province, China. Then, the prepared zircon grains were handpicked, embedded in epoxy resin, and polished to expose the grain centers. Zircons that were free of visible inclusions and fractures were selected for cathodoluminescence (CL) imaging in the electron microprobe laboratory at the State Key Laboratory of Geological Processes and Mineral Resources (GPMR), China University of Geosciences (CUG), Wuhan.

Measurements of U, Th, Pb isotopes and trace elements in the zircons were performed synchronously by using a laser ablation inductively coupled plasma mass spectrometer (LA–ICP–MS) at GPMR. Laser sampling was conducted by using GeoLas 2005 with a beam diameter of 32 μm, and an Agilent 7500a ICP–MS instrument was used to acquire ion-signal intensities. Helium was used as a carrier gas, while argon was used as a make-up gas. The two gases were mixed before entering the ICP. We analyzed the standards 91500 and GJ-1 for U-Pb dating and NIST 610 as an external standard for trace element analyses. Each analysis incorporated a background acquisition of 20 s followed by 60 s of data acquisition from the sample. The detailed work conditions for the laser ablation system and the ICP–MS instrument were described by Liu et al. (2010). Software *ICPMSDataCal* was used for the off-line selection and integration of background and analytical signals, and time-drift correction and quantitative calibration were applied for the trace element analyses and U–Pb dating (Liu et al., 2010). Concordia diagrams and weighted mean calculations were conducted by using Isoplot Version 3.75 (Ludwig, 2012).

4.2. Major and trace element determination

Fresh whole-rock samples were crushed in a corundum jaw crusher and powdered to less than 200 mesh by an agate ring mill. The major elements were analyzed by using X-ray fluorescence (XRF) spectrometer at the Australian Laboratory Services' (ALS) Chemex (Guangzhou) Co. Ltd. The analytical precision is better than 5 % for most major elements. Prepared samples for the trace element analyses were digested by $HF+HNO_3$ in Teflon bombs and analyzed with an Agilent 7500a ICP–MS at the GPMR. The detailed sample-digesting procedure for the ICP–MS analyses and the analytical precision and accuracy for the trace elements are the same as described by Liu et al. (2008b).

4.3. Sr–Nd isotope analyses

The Sr–Nd isotope compositions were determined at the GPMR in CUG by using a Finnigan MAT 261 thermal ionization mass spectrometer (TIMS). Sample powders were spiked with mixed isotope tracers (^{84}Sr, ^{85}Rb, ^{145}Nd and ^{149}Sm) and dissolved in Teflon screwtop beakers with $HCl+HClO_4/HNO_3$ acids. Isotope separation was performed with conventional cation-exchange techniques. The procedural blanks were below 0.05 ng for Sm and Nd and below 0.20 ng for Rb and Sr. The measured isotopic ratios of the standard samples were 0.710236 ± 16 (2σ) for $^{87}Sr/^{86}Sr$ (NBS987), and 0.512620 ± 2(2σ) for $^{143}Nd/^{144}Nd$ (BCR-2). The $^{143}Nd/^{144}Nd$ values of the samples were normalized to $^{146}Nd/^{144}Nd = 0.7219$, and the $^{88}Sr/^{86}Sr$ ratios were corrected to $^{88}Sr/^{86}Sr = 8.3752$. The precisions for $^{87}Rb/^{86}Sr$ and $^{147}Sm/^{144}Nd$ are better than 1 % and 0.5 %, respectively (Gao et al., 2004).

4.4. In situ Hf isotope determination

In situ Lu–Hf isotope analyses were conducted in dated zircon grains with identical sampling spots to the U-Pb analyses or within the same oscillatory zones. A Neptune Plus MC-ICP-MS (Thermo Fisher Scientific, Germany) equipped with a GeoLas 2005 excimer ArF laser-ablation system (Lambda Physik, Göttingen, Germany) was used at GPRM. The sampling-spot size was 44 um, and the energy density was 15–20 J/cm^2 during the analyses. The standards 91500 and GJ-1 were simultaneously analyzed (Hu et al., 2012). The obtained Hf isotope compositions were 0.282315 ± 0.000014 (1σ) for 91500 and 0.282019 ± 0.000013 (1σ) for GJ-1. The off-line selection and integration of analytical signals and mass-bias calibrations were conducted by using *ICPMSDataCal* (Liu et al., 2008a).

5. Results

5.1. Zircon U–Pb isotope and trace element compositions

The zircon U–Pb isotope and trace element data from the Xiangride granodiorite (B1009-1; N35°54'45.30", E97°58'57.10") and Asiha quartz diorite (B1001-1; N35°49'36.20"; E98°16'01.60") are presented in tables S1 and S2. Representative CL images of the zircons are shown in Fig. 4. The zircon grains that were extracted from the Xiangride granodiorite are dominated by prismatic shapes and are transparent and colorless. Their crystal sizes range from 80 to 600 um and their aspect ratios range from 1.5:1 to 6:1. The distinct oscillatory zonings (Fig. 4A) and high Th/U ratios (0.59–0.92; table S1) of these zircons suggest magmatic origin. Eighteen spots on zircons from the granodiorite reveal a

$^{206}Pb/^{238}U$ age population of ca. 240–244 Ma and produce a weighted mean age of ca. 242 ± 1 Ma (MSWD = 0.26; n = 18; Fig. 4C). The rare earth element (REE) patterns of the zircons from the granodiorite are scattered and show negative Eu anomalies and weakly positive Ce anomalies (Fig. 5A).

The zircons from the quartz diorite are transparent and colorless. The crystals are euhedral and prismatic with various lengths of 150–300 um and aspect ratios from 1:1 to 3:1. All the zircons display clear oscillatory zonings around dark cores (Fig. 4B) and show high Th/U ratios (0 0.35–0.73; table S1), indicating a magmatic origin. Twenty-two spots were analyzed on both the mantles and cores of zircons from the quartz diorite. The ages of these mantles and cores show no systematic distinction, yielding an $^{206}Pb/^{238}U$ age population of ca. 239–245 Ma and a total weighted mean age of ca. 242 ± 2 Ma (MSWD = 0.093; n = 22; Fig. 4D). Previous dating results from quartz diorite, which produced ages of 238–244 Ma (B.Y. Li et al., 2012; J.C. Li et al., 2014), were similar to our dates, so we can consider ca. 242 Ma as the crystallization age of the quartz diorite. Compared to the REE features of the zircons from the Xiangride granodiorite, all the analyses of the zircons from the Asiha quartz diorite show nearly coherent chondrite-normalized REE patterns and obvious enrichment in heavy rare earth elements (HREEs; Fig. 5B). Distinct positive Ce (Ce/Ce*=43 on average) anomalies and negative Eu anomalies (Eu/Eu*=0.23 on average) are also observed (Fig. 5B).

5.2. Major and trace element geochemistry

The major and trace element analytical results are presented in table S3 and illustrated in Figs. 6–8. Compared to the quartz diorite discussed below, the Xiangride granodiorite is

characterized by relatively high SiO_2 (66.00–72.50 wt. %) and K_2O (2.31–4.09 wt. %) and low Al_2O_3 (14.25–16.45 wt. %), Na_2O (3.60–4.09 wt. %), CaO (1.89–4.21 wt. %), MgO (0.43–1.34 wt. %) and Fe_2O_3 (2.24–3.55 wt. %) with Mg# values of 27.7–45.9. These signatures denote the granodiorite as metaluminous–slight peraluminous high-K calc-alkalic granodiorite–granite (Fig. 6 and table S3). The major oxides, except for K_2O, show negative correlations with SiO_2 (Fig. 7). These trends may indicate the fractional crystallization of hornblende, biotite and plagioclase during magma evolution. Additionally, the granodiorite displays enrichment in LREEs and LILEs, depletion in HREEs and HFSEs (such as Nb, Ta, P and Ti), high $(La/Yb)_N$ ratios (21.2 on average) and slight-moderate Eu anomalies (Fig. 8A–B). The relatively wide compositional ranges of these samples, especially the Mg# (27.7–45.9) and Eu anomalies (0.50–0.91), could have resulted from the fractionation of plagioclase and mafic minerals, considering that the high-silica samples show more significant Eu anomalies and lower Mg#. This contention is also consistent with micro petrography studies, which indicated more K-feldspar and quartz and less plagioclase and amphibole in these high-SiO_2 samples.

The MMEs from the granodiorite exhibit low SiO_2 (54.90–59.10 wt. %), high Fe_2O_3 (6.06–7.50 wt. %), and moderate MgO (3.07–3.67 wt. %) with Mg# values of 38.0–50.0. These enclaves are metaluminous and alkali-calcic and thus can be classified as monzonite–monzo-diorite (Fig. 6). These enclaves also exhibit enrichment in LREEs and LILEs, depletion in HREEs and HFSEs, and moderate Cr (10.0–16.6 ppm) and Ni (8.0–14.1 ppm) contents, which are similar to those of the Annage hornblende gabbro from the Gouli area

(table S3 and Fig. 8C–D).

The samples from the Asiha quartz diorite exhibit intermediate compositions with restricted SiO_2 contents between 59.00 and 62.49 wt. %. These samples contain 2.66 to 3.38 wt. % MgO and 5.09 to 6.29 wt. % $Fe_2O_3^T$ with Mg# values from 49.5 to 52.9. They have relatively high concentrations of Na_2O (3.40–3.54 wt. %), CaO (5.29–5.97 wt. %) and Al_2O_3 (16.85–17.40 wt. %) and moderate K_2O (2.00–2.58 wt. %), indicating medium- to high-K, calc-alkalic and metaluminous features (Fig. 6). The chondrite-normalized REE patterns of the Asiha quartz diorite display that all samples are enriched in LREEs with respect to HREEs and show slightly negative Eu anomalies (Eu/Eu^* between 0.73–0.83), similar to bulk CC (Fig. 8C and table S3). Their $(La/Yb)_N$ ratios range from 10.2 to 16.5 and are higher than that of lower CC (5.3; Rudnick and Gao 2003). The quartz diorite also exhibits enrichment in LILEs (such as Rb, Th, U, K and Pb) and depletion in HFSEs (including Nb, Ta, Ti, P, Zr and Hf) and has moderate Cr (31.2–31.3 ppm) and Ni (15.3 ppm; Fig. 8D and table S3) contents, resembling bulk CC.

5.3. Sr and Nd isotopes

Sr–Nd isotope compositions are presented in table S4 and illustrated in Fig. 9A. The Xiangride granodiorite displays variations in Sr–Nd isotope compositions that are characterized by $(^{87}Sr/^{86}Sr)_i$ = 0.708835–0.713553, $\varepsilon_{Nd}(t)$ from -6.8 to -5.3, and $T_{2DM}(Nd)$ = 1218–1908 Ma. Among the granodiorite samples, sample B1005-1 show relatively high $(^{87}Sr/^{86}Sr)_i$ (0.713553), which could be caused by local post-magmatic weathering considering that some fine weathering minerals have been found within mafic minerals

(e.g., biotite; Fig. 3D) and/or error propagation given the relatively high $^{87}Rb/^{86}Sr$ (3.3527) of this sample (Wu et al., 2000). The MMEs from the granodiorite show $(^{87}Sr/^{86}Sr)_i$ from 0.708167 to 0.709613 and $\varepsilon_{Nd}(t)$ = -6.4 to -5.4, similar to the host rocks, but older $T_{2DM}(Nd)$ (1541–2115 Ma). These Sr–Nd isotope compositions are distinguished from mid-ocean ridge basalt (MORB), ocean island basalt (OIB) and supracrustal rocks (Fig. 9A). The parameters of the Asiha quartz diorite are also similar to those of MMEs, with $(^{87}Sr/^{86}Sr)_i$ = 0.708805–0.709107, $\varepsilon_{Nd}(t)$ from -5.6 to -5.7, and $T_{2DM}(Nd)$ = 1523–1533 Ma.

5.4. Zircon Lu–Hf isotopes

The Hf isotopic data of zircons from the Xiangride granodiorite and Asiha quartz diorite are listed in table S5 and illustrated in Fig. 9B–C. The granodiorite has variable $^{176}Hf/^{177}Hf$ ratios (0.282635–0.282775), with $\varepsilon_{Hf}(t)$ values from 0.3 to 5.1 and T_{2DM}^{C} = 857–1122 Ma, which are identical to the slab-derived granodiorite from the Dulan (Huang et al., 2014). The quartz diorite has homogeneous $^{176}Hf/^{177}Hf$ ratios (0.282578–0.282646), with $\varepsilon_{Hf}(t)$ values from -1.6 to 0.7. The T_{2DM}^{C} of the rock is 1103–1230 Ma, similar to those of enriched mantle-derived lamprophyres (Xiong et al., 2013).

6. Discussion

All the rocks from the Gouli batholith display medium–high K, calc-alkalic and metaluminous to slightly peraluminous characteristics and show rare earth element and trace element patterns that are consistent with those of bulk CC (Figs. 6 and 8). This result offers an opportunity to examine the mechanism of the growth of CC. A comprehensive

investigation of tectonic setting and origin of the batholith is required to detail this process.

6.1. Subduction setting of the Gouli batholith

Multiple lines of research progress from regional magmatic rocks, metamorphism, unconformities, and the sedimentary facies of strata across the EKOB between the Permian and Triassic provide us an opportunity to decipher the exact formation setting of the Gouli batholith. The Halaguole and Dur'ngoi ophiolites that are exposed in the SEKS reveal that the A'nyemaqen Ocean opened at ca. 345Ma (Chen et al., 2001; Liu et al., 2011). The deficiency of arc-type magmatic rocks between 330 and 260 Ma in the EKOB (Figs. 1B and 10) implies that the subduction of the ocean did not initiate until 260 Ma or that the subduction was in an early stage, when the dip angle of the subduction plate was small. The earliest arc-type magmatic rocks in the EKOB (261±2 Ma) indicate that oceanic subduction should not have initiated later than 261Ma (Xiong et al., 2012). The following oceanic subduction is further evidenced by giant igneous rocks between 260 Ma and 237 Ma, including arc-related granitoids with MMEs (Liu et al., 2004; Huang et al., 2014; Xiong et al., 2014), mafic dikes and intrusions (Xiong et al., 2011; Xiong et al., 2011) and widespread volcanic rocks (Figs. 1B and 10; Ni, 2010; Xiong, 2014), and by the subduction-related metamorphism features in schist (246 Ma; Chen et al., 2007c). Although the termination time of subduction and the initiation of collision cannot be precisely constrained by arc-related granitoids, post-orogenic extension-related A-type adamellite (231±4 Ma; e.g., Xi et al., 2010) in the NEKT clearly reveals that the A'nyemaqen Ocean should have closed earlier than ca. 231 Ma.

Further evidence that constrains the closure time of the A'nyemaqen Ocean can be found from the unconformities and sedimentary facies of the regional strata in the EKOB. Given the inevitable intense compression from the subduction of the ocean and continent-continent collision, oceanic subduction and closure are usually accompanied by the formation of regional unconformities. Three unconformities between 260 and 231 Ma were identified (Fig. 10) in the EKOB. The first angular unconformity, which is below the Late Permian Gequ Formation (deposited during 260–252 Ma; Fig. 10), was emphasized by Huang et al. (2014) as the initial record of the collision, but a specific study revealed that the Gequ Formation, which consists of molasse sediments was deposited in an oceanic environment (R.B. Li et al., 2012). The appearance of marine sediments above this angular unconformity further indicates that the A'nyemaqen Ocean still existed after the intense tectonic movement, as recorded by the molasse sediments from the Gequ Formation (Fig. 10). Thus, initial A'nyemaqen Ocean subduction was more than likely responsible for the angular unconformity and molasse deposits. This speculation is also supported by the occurrences of arc-related magmas at the same time as the unconformity (discussed above; Fig. 10). The second unconformity is a micro angular unconformity between the Naocangjiangou Formation and Xilikete Formation, both of which show marine facies, precluding the possibility that the A'nyemaqen Ocean closed during the forming of this unconformity (Figs. 2 and 10). The third unconformity is a regional angular unconformity (Figs. 2 and 10). The Xilikete Formation below this unconformity consists of marine sediments, while the Babaoshan Formation above the unconformity consists of lake or river

sediments (Figs. 2 and 10). These indicate that ocean-continent conversion occurred during the formation of this unconformity and the ocean had disappeared before the sedimentation of the Babaoshan Formation (ca. 237 Ma). Thus, the subduction of the A'nyemaqen Ocean had ceased by ca. 237 Ma because of the closure of the ocean, which is consistent with the conclusion from the regional magmatism.

In summary, we contend that the A'nyemaqen Ocean subduction initiated at ca. 260 Ma, while the closure of the ocean and initial collision between the BHT and SEKT occurred at ca. 237 Ma along the SEKS. Thus, the 260–237 Ma granitoids throughout the EKOB, which also include the ca. 242 Ma Gouli batholith, must have formed during the subduction of A'nyemaqen Ocean instead of syn-collision between the BHT and SEKT, as proposed by Huang et al. (2014) and Shao et al. (2017).

6.2. Petrogenesis of the Gouli batholith

The Gouli batholith mainly consists of the Xiangride granodiorite, Asiha quartz diorite and MMEs. The composition variations of the contemporaneous magmatic rocks may imply a complex genesis.

6.2.1. Petrogenesis of the MMEs and mafic magma source

MMEs are prevalent in I-type granitoids (Vernon, 1984; Didier and Barbarin, 1991; Barbarin, 2005) and can be explained as xenoliths of country rocks, restites from their source regions (Charan et al., 2009; Zhao et al., 2012), cumulates (Dorais et al., 1997), autoliths (Barbarin, 2005) or mafic magma blobs that became mixed with their host magma (Holden et al., 1987; Fu et al., 2016).

The MMEs within the Gouli batholith are rounded, ellipsoidal and elongated without solid-state deformation (Fig. 3B and I). These petrographic characteristics indicate their coeval nature with the host magma before the MMEs were solidified (Kumar et al., 2004) and preclude a xenolith or restite model for the MMEs (Vernon, 1984). This conclusion is also supported by their fine-grained igneous rather than metamorphic textures (Fig. 3E–I), plagioclase xenocrysts with hornblende inclusions and sharp-contact overgrowth rims (Fig. 3H). The above petrographic characteristics and the eroded plagioclase in the MMEs also preclude a cumulate or autolith model for the MMEs (Fig. 3F–I), because cumulates or autoliths always equilibrate with the evolving magma and lack eroded plagioclase. Actually, the acicular apatite in the MMEs (Fig. 3I) and chilled margins between the MMEs and their host rocks (Fig. 3E and I) are similar to those of most of the MMEs in the EKOB (Liu et al., 2004; Xiong, 2014), indicating that these rocks formed when hot mafic magma was injected into cold silicic magma. This conclusion is further evidenced by the geochemical signatures of the MMEs and their host rocks. Compared to the host rocks, the Nb/Ta, Sr/Y and La/Yb ratios of the MMEs (11.3–16.7, 16.0–28.0, 8.0–15.1, respectively) are notably distinct from those of the host rocks (9.3–11.2, 6.3–64.2, 10.1–46.2, respectively), indicating that another source was necessary for the MMEs in addition to the granodiorite magma. The different patterns of the REE and trace element diagrams between the MMEs and the host granodiorite may also preclude that these rocks originated from the same source (Fig. 8). The linear geochemical trends for the enclaves and host rocks may also represent a two-component mixing model (Fig. 7). Moreover, if the MMEs are cumulates of the host

granodiorite, the fractionation of a large amount of amphibole and plagioclase (represented by the mineral compositions of the MMEs) from the granodiorite magma would slightly increase the Sr/Y and $(La/Yb)_N$ ratios with increasing SiO_2 content (Xu et al., 2015; Dai et al., 2016) because amphibole has higher compatibility with Y and Yb than Sr and La in calc-alkaline magmas (Nandedkar et al., 2016). However, in our study, the Sr/Y and $(La/Yb)_N$ ratios display negative relationships with SiO_2 (Fig. 11), arguing against the cumulate model. Thus, a genetic model that describes mixing between mafic magma and more silicic magma for the MMEs from the Gouli batholith is appropriate.

Although the MMEs cannot represent the primitive composition of the mafic magma end-member because of the effect of magma mixing, the different compositions of the MMEs compared to the host rocks can still provide useful information regarding their source. The MMEs show moderate SiO_2, Cr, Ni and MgO contents and high Mg# values (48–51), the latter of which are similar to the enriched mantle-derived basic dikes (Mg#=50–55) from the EKOB (Xiong, 2014). This result may indicate the involvement of mantle components in the mafic magma source (table S3). Enriched mantle should be an appropriate source because of the arc magma affinities of these rocks (high HREEs and LILEs, distinctly negative Nb, Ta and Ti anomalies, and low Sr/Y and $(La/Yb)_N$ ratios; Figs. 8A–B and 12A–B). In addition, the MMEs have high Nb contents (11.71–22.83ppm; table S5) and high Nb/La (0.7–1) and Nb/U (7.7–9.3) ratios, which are similar to those of the Nb-enriched basalts and different from those of “normal” arc basalt-basaltic andesite (Kepezhinskas et al., 1996; Castillo, 2012). Considering the mixing with low-Nb felsic magma as represented by the granodiorite

magma (discussed below), the Nb contents of the primitive mafic magma should be higher. These geochemical signatures together with the low Zr abundances (128.25–169.29ppm), the low Zr/Y ratios (4.0–8.3) and the negative Eu anomalies indicate that the mafic magma originated from the partial melting of mantle-wedge peridotite that was metasomatized by slab-derived fluids (S.M. Li et al., 2014). Moreover, the appearance of the coeval enriched mantle-derived Annage hornblende gabbro in the study area (Fig. 1C), their similar mineral assemblages, and accordant REE and trace element patterns (Fig. 8A–B) and Sr-Nd signatures (Fig. 9A) imply that the mafic magma may have had the same source as the enriched mantle-derived Annage hornblende gabbro (Fig. 1C). In conclusion, the primitive mafic magma of the MMEs should have been derived from the enriched mantle, and the MMEs are the mixture of enriched mantle-derived melt and slab-derived magma.

6.2.2. Petrogenesis of the Xiangride granodiorite and felsic magma source

Field observations revealed that the MMEs in the Xiangride granodiorite are much sparser and smaller than those in the Asiha quartz diorite (Fig. 1A–C and J). This phenomenon and the relatively silicic signatures of the granodiorite, imply that the input of mafic magma may have had a limited effect on the chemical composition of the granodiorite magma compared to the diorite magma. This conclusion is also supported by the petrographic characteristics of the granodiorite and MMEs. As shown in the hand specimens and under a microscope, abundant plagioclase and quartz xenocrysts occur in the MMEs from the Xiangride granodiorite (Fig. 3C and H). This result indicates that the felsic magma was already a crystal-enriched melt when the mafic magma was injected into.

Although chemical exchange is inevitable between residual liquid melts and mafic magmas, magma mixing may have a limited effect on the compositions of the host rocks because granitoid magmas under sub-liquidus conditions are “crystal mashes” and element diffusion is restricted by the inefficient diffusion (Ramos and Reid, 2005; McLeod et al., 2012). Moreover, the notable chemical composition gaps between the granodiorite and MMEs in the Harker diagrams (Fig. 7) also support the above conclusion. In summary, the Xiangride granodiorite, although affected by magma mixing, still remains significant information of a felsic magma end-member and can shed light on its origin.

The granodiorite shows high SiO_2 (66.00–72.50 wt. %), low MgO (0.43–1.34 wt. %), moderate Mg# values (27.7 to 45.9), and low Cr (1.37–8.15 ppm) and Ni (0.99–6.72ppm), suggesting that the felsic magma end-member was not directly derived from the partial melting of mantle peridotite (Castillo, 2012). On the other hand, the granodiorite samples generally show low amounts of garnet-compatible elements (HREEs), high abundance of Sr, and high Sr/Y and $(La/Yb)_N$ ratios (table S3), similar to adakites (Fig. 12A and B; Defant and Drummond, 1990). However, two granodiorite samples (B1005-1 and B1009-1) display relatively low Sr/Y and $(La/Yb)_N$, which obscure the adakitic nature of the intrusion. Plots of the Sr/Y and $(La/Yb)_N$ ratios and the Sr and Y contents against SiO_2 are shown in Fig. 11 to decipher the relatively low Sr/Y ratios of samples B1005-1 and B1009-1. The Sr/Y ratios and Sr contents show negative relationships with SiO_2, while the Y contents display the opposite trend. These results suggest that the Sr/Y ratios decreased as the granodiorite magma evolved, which should have been caused by the increasing Y and decreasing Sr contents from

crystal fractionation. Thus, the relatively low Sr/Y ratios of samples B1005-1 and B1009-1 should have been caused by magma evolution, given their relatively high silica contents, and the granodiorites should be adakites or adakitic rocks. This type of rock can be produced by various processes, including the melting of thickened or foundering lower CC (Gao et al., 2004; Wang et al., 2005), the assimilation and fractional crystallization of basaltic magma (AFC; Castillo et al., 1999; Macpherson et al., 2006; Castillo, 2012), and the melting of the subducting slab (Defant and Drummond, 1990; Rapp et al., 1999).

Magma from thickened lower CC may exhibit low MgO, Cr, Ni and Y contents, high Sr contents, high Sr/Y ratios, and radiogenic Sr-Nd isotopes, which are all observed in the granodiorite (tables S3 and S4). However, the εHf(t) values of the granodiorite show an apparent depleted characteristic (0.3 to 5.1; table S5) that cannot be explained by the thickened lower CC model or the involvement of subcontinental mantle-derived magma into the source of lower CC because of the relatively radioactive Hf isotopes of the enriched mantle as revealed by the immediately adjacent Annage hornblende gabbro (Fig. 9B; εHf(t)= -4.9 – -0.4). Thus, a lower CC source is not appropriate for this granodiorite. This conclusion is also supported by the following lines of evidence: (1) the contemporaneous (250–238 Ma) granitoids in the EKOB, which originated from lower CC (e.g., Song et al., 2013; Yin et al., 2013; Xiong et al., 2014), show distinguishably lower Sr/Y and $(La/Yb)_N$ ratios, which preclude crustal thickening during this period; and (2) as discussed in section 6.1, the granodiorite intruded before continental collision, during which the CC should have exhibited normal thickness (Fig. 12D). Magma that was sourced from foundering lower CC is

an alternative source, but this scenario would normally lead to the formation of high-Mg# andesite or intrusive counterparts, which have not been found in the EKOB (Gao et al., 2004). In addition, lithospheric delamination in an orogenic belt should lead to coeval extension-related metamorphism (Sacks and Secor, 1990; Li et al., 2002), which have not been found in this area. Moreover, the Gouli batholith formed in a subduction setting as discussed above, which is inconsistent with a delamination-related extensional regime. Consequently, the partial melting of thickened or foundering lower CC is not suitable for the formation of the Xiangride granodiorite.

AFC is another possible mechanism that can explain the major and trace element signatures of the granodiorite. However, assimilation of CC would create a positive correlation between $(^{87}Sr/^{86}Sr)_i$ and SiO_2 and a negative correlation between $\varepsilon_{Nd}(t)$ and SiO_2, which are not observed in the granodiorite (table S4). The lack of ancient inherited zircons may also be inconsistent with the assimilation of basaltic magma (Fig. 4). The fractionation of amphiboles was proposed for elevated Sr/Y and $(La/Yb)_N$ ratios in evolving magma (Chen et al., 2016) and has been applied to many case studies (e.g., Xu et al., 2015), but amphibole fractionation typically occurs with plagioclase which may negate the effects of amphibole as revealed in a previous study, and thus may have had a limited effect in creating adakitic signatures (Moyen, 2009). Moreover, if the high Sr/Y and $(La/Yb)_N$ ratios were induced by the fractionation of amphibole, a positive relationship between Sr/Y or $(La/Yb)_N$ and fractional crystallization indices (e.g., SiO_2) should have been observed in our study (Xu et al., 2015; Dai et al., 2016) because of the higher amphibole-liquid partition coefficients of Y and

Yb compared to those of Sr and La in calc-alkaline magmas (Nandedkar et al., 2016). However, our data show opposite trends (Figs. 11A and B), arguing against the above conclusion.

Accordingly, the melting of the subducting slab should be an appropriate model for the generation of the granodiorite. The subducting slab constitutes at least two chemically different ingredients: basaltic oceanic crust and more silicic overlying sediments (Tatsumi, 2006). Melt from the slab would manifest geochemical signatures between the two end-members (Huang et al., 2014). Compared to the enriched mantle-derived Annage hornblende gabbro, the distinctly positive $\varepsilon_{Hf}(t)$ values of the granodiorite suggest that an isotopically depleted source (with more depleted $\varepsilon_{Hf}(t)$ than the enriched mantle) was required (table S5 and Fig. 9B). Actually, the granodiorite displays positive $\varepsilon_{Hf}(t)$, similar to the slab-derived magma as revealed by the Dulan granodiorite (Fig. 9B; Huang et al., 2014), implying that subducting oceanic crust is a potential candidate. This conclusion is supported by additional lines of evidence. Compared to the adjacent enriched mantle-derived Annage hornblende gabbro, the higher Sr/Y ratios (averaging 47) of the granodiorite, which were not caused by amphibole fractionation (discussed above), should indicate a deeper source than that of the mantle-derived Annage intrusion (Chapman et al., 2015; Chiaradia, 2015; Dai et al., 2016). Thus, a subducting slab source below subcontinental mantle should be the most plausible candidate. In addition, the Sr/Y ratios and Y contents of the granodiorite can be well modelled by the partial melting of MORB with residues of eclogite and 10 % garnet amphibolite, and the calculated $(La/Yb)_N$ and Yb_N values of the granodiorite are also in

conformity (Fig. 12A–B). This conclusion is also supported by the fact that all the samples from the granodiorite plot in the field of metabasaltic and eclogite melts in the Mg# vs. SiO_2 diagrams (Fig. 12C).

However, the partial melting of oceanic crust cannot solely explain all the geochemical features of the granodiorite. The high LILEs, including the Pb and LREEs, and low Mg contents and Mg# values imply that a crustal end-member may have been involved in the primary magma (Fig. 8). The relatively high K_2O/Na_2O (0.6–1.1) and low Mg# of the granodiorite may have required a high-K_2O/Na_2O and low-Mg# materials in the source region. The contamination of CC or the partial melting of continent-derived subducting sediments atop the oceanic crust can explain these geochemical signatures. The contamination model creates a positive correlation between $(^{87}Sr/^{86}Sr)_i$ and SiO_2 and a negative correlation between $\varepsilon_{Nd}(t)$ and SiO_2 for the resultant magma, which are not observed in the granodiorite (table S4). Additionally, the relatively low K_2O/Na_2O (0.6; Rudnick and Gao, 2003) of the CC cannot explain the relatively high K_2O/Na_2O of the granodiorite. Thus, subducting terrigenous sediments with lower Mg# (41-46) and relatively higher K_2O/Na_2O (0.8–1.6; Shimoda et al., 1998) are the most plausible crustal end-member for the granodiorite magma. Some additional evidence below should also support this conclusion. First, the relatively enriched Sr-Nd isotopes of the granodiorite compared with the MORB reveal the possible involvement of subducting sediments. A “mixing” model that applies Sr-Nd isotope data from the oceanic crust as defined by 350 Ma A’nyemaqen MORB (Guo et al., 2007) and subduction sediments as defined by Shaliuhe granitic gneiss (Meng et

al., 2005; Chen et al., 2007) can perfectly explain the Sr-Nd isotopic signatures of the Xiangride granodiorite. In this model, 60–70 % MORB contribution and ca. 30–40 % terrigenous sediments are required to reach mass balance (Fig. 9A). In addition, the scattered and old T_{2DM}(Hf) of the granodiorite (857–1122Ma; table S5) is similar to the age of the Shaliuhe granitic gneiss (774–1399 Ma; Chen et al., 2007), further indicating that the required sediment may have involved supracrustal materials from the weathering of the Shaliuhe granitic gneiss (Huang et al., 2014). Moreover, we used Hf isotopes to verify the "mixing" trend between the two above end-members discussed above and the proportion of the required subducting sediments (Fig. 9C). In terms of the Hf isotopic model, the εHf(t) of the MORB was calculated based on the method suggested by Chauvel et al. (2008) since no Hf isotopic compositions of the A'nyemaqen MORB (mantle end-member in the model) have been reported. For our samples, we used the initial Hf of the zircons to represent the whole-rock initial Hf compositions. Although the model based on these data is not rigorous, it can still roughly indicate that a proportion of ca. 30–40 % terrigenous sediments is necessary to be involved in the source to lower the εHf(t) of the resultant magma from >15 (pure basaltic oceanic crust-derived magma) to 0.3–5.1 (granodiorite from basaltic oceanic crust and overlying terrigenous sediments). Additionally, decoupling occurred between Nd and Hf isotopes. This phenomenon can be caused by many processes (Hoffmann et al., 2011; Vervoort et al., 2011). In our study, the Hf–Nd compositions are above the terrestrial array (Fig.9 C). This could be related to the involvement of both marine sediments and basaltic oceanic crust in the magma source (Vervoort et al., 2011), which is consistent with our

conclusion.

Thus, we propose that the Xiangride granodiorite was derived from the partial melting of subducting oceanic crust and overlying sediments, and fractional crystallization should have played a role in the magmatic evolution according to the linear trends of the major elements in the Harker diagrams (Fig. 7) and the wide ranges of the SiO_2 and Mg# values (table S3). As discussed above, the Xiangride granodiorite can roughly represent the felsic magma end-member of the Gouli batholith, so the primitive felsic magma of the batholith is slab-melt. The high Sr/Y and $(La/Yb)_N$ ratios of the granodiorite magma, which may be higher, considering the crystal fractionation (Fig. 11), should indicate that the residue in the source region was eclogite or garnet-bearing amphibolite (Fig. 12A–C).

6.2.3. Petrogenesis of the Asiha quartz diorite

The quartz diorite displays similar geochemical characteristics to the MMEs and thus cannot be explained by solely felsic magma or mafic magma (table S3 and Fig. 7). Considering the same crystallization ages of the quartz diorite, the Xiangride granodiorite and Annage hornblende gabbro, we propose that the quartz diorite is the product of mixing between the felsic magma end-member and mafic magma end-member as discussed above. This result is supported by the following lines of evidence. First, the contents of most of the major elements in the quartz diorite are between those in the Annage hornblende gabbro and Xiangride granodiorite (Figs. 7 and 9B), and are similar to those in the MMEs. These geochemical trends can be explained by the mixing model. In addition, the Sr-Nd isotopic compositions of the slab-derived magma (represented by the Dulan granodiorite; Huang et

al., 2014) and subcontinental mantle-derived magma (represented by the adjacent Annage hornblende gabbro and lamprophyres; Zhao et al., in press; Xiong et al., 2013) are similar (Fig.9 A). This similarity should have been caused by multiple stages of enrichment in the subcontinental mantle that were related to the subduction of the Proto-Tethys Ocean and Paleo-Tethys Ocean (A'nyemaqen Ocean) and could have caused the quartz diorite, which originated from mixing of the two sources, show similar Sr-Nd compositions to those of granodiorite. Thus, detecting the proportions of different sources that were involved in the resultant magma by using the Sr-Nd compositions is difficult, but the identical Sr-Nd isotopes of the quartz diorite and MMEs still imply the possibility that the quartz diorite formed by mixing of slab-derived magma and subcontinental mantle-derived magma. Moreover, the diagnostically moderate $\varepsilon_{Hf}(t)$ (-1.6–0.7) values of the quartz diorite, which fall between those of the slab-derived granodiorite and the adjacent subcontinental mantle-derived Annage hornblende gabbro, indicate the involvement of low-$\varepsilon_{Hf}(t)$ magma from the enriched subcontinental mantle is reasonable (Fig. 9B). Additionally, the enclaves within the quartz diorite are much denser and larger than those within the granodiorite (Fig. 3A, B and J). This should indicate the quartz diorite magma was closer to the hot mafic magma than the granodiorite (Fig. 13) and that more intensive mixing occurred (Kumar and Rino, 2006), which matches the lower SiO_2 and higher MgO, Cr, Ni and Mg# of the quartz diorite compared to the granodiorite. Furthermore, the REE and trace element patterns of the Asiha diorite are similar to those of the MMEs, which may imply a similar petrogenesis. In summary, we contend that mixing between the slab-derived and enriched mantle-derived

melts generated the Asiha quartz diorite.

6.2.4. Genetic model for the Gouli batholith

Based on the petrography, geochemical data and Sr-Nd-Hf isotopic compositions of the Xiangride granodiorite, MMEs, and Asiha quartz diorite, a complex and multi-stage model that includes partial melting, magma mixing and crystal fractionation during subduction is proposed for the Gouli batholith (Fig. 12D). The granodiorite, which has high SiO_2, low Cr, Ni, MgO and Mg#, and higher $\varepsilon_{Hf}(t)$ compared to the enriched mantle-derived Annage hornblende gabbro, formed through the partial melting of the subducting oceanic crust (60–70 %) and terrigenous sediments (30–40 %), coupled with crystal fractionation as evidenced by the negative Eu anomalies (Fig. 8A). The primary magma of the MMEs and Asiha diorite, which have moderate MgO, Cr, Ni and Mg# and enriched $\varepsilon_{Hf}(t)$, was derived from the subcontinental mantle. Inevitable fractional crystallization should have also played a role in the magma's evolution. The evolving magma ultimately mixed with the felsic magma, and the resultant magma formed the MMEs and Asiha quartz diorite.

As shown in Fig. 13, the processes that generated the Gouli batholith can be summarized as follows: (1) the partial melting of the subducting oceanic crust and the overlying terrigenous sediments generated the felsic magma (Fig. 13A); (2) the felsic magma ascended and assembled, forming a magma chamber within the crust; (3) the enriched mantle-derived mafic magma was injected into the crystallizing slab-derived felsic magma chamber, and a hybrid magma zone formed between the contact area of the two magma end-members (Fig. 13B); (4) Basic and hybrid globules were further forcibly injected,

mingled and dispersed into/in the relatively cooler felsic melts (Fig. 13B) because of the convection of the magma, and crystals such as plagioclase were transferred from the felsic magma into the hybrid globules (MMEs) and acted as xenocrysts in the MMEs; additionally, chemical and mechanical exchanges occurred at the same time; (5) the felsic magma, hybrid magma from the hybrid zone, hybrid globules and mafic magma ultimately formed the granodiorite, quartz diorite, MMEs and hornblende gabbro, respectively, as the ascending of the magmas and decreasing in magma temperature (Fig. 13A).

6.3. Implications for continental crustal growth

A "continental collision zone model" has been proposed for CC growth (Mo et al., 2008; Niu et al., 2013) and has been applied to the Gangdese magmatic belt (Mo et al., 2008), Qilian Orogen (Zhao et al., 2017) and EKOB (Huang et al., 2014; Shao et al., 2017). Indeed, some of granitoids with CC-like signatures formed in a collision setting (Gao, 2013) contributing to CC growth in the EKOB. However, as discussed above, the chemically crust-like Gouli batholith and most of the Permian–Triassic granitoids in the EKOB (260–237 Ma; Figs. 8 and 10; e.g., Xiong, 2014) were produced in a subduction setting, which is inconsistent with this "continental collision zone model" (Niu et al., 2013). On the other hand, the felsic Xiangride granodiorite in the Gouli batholith displays high Sr/Y and depleted Hf isotope signatures, indicating that depleted oceanic crustal materials were involved in the formation of the batholith, while the intermediate Asiha diorite and MMEs show relatively enriched Sr-Nd-Hf isotope characteristics, suggesting the involvement of subcontinental enriched mantle materials in the source. Both slab and subcontinental

mantle contributed to the formation of the Gouli Batholith and probably the ubiquitous Permian–Triassic granitoids (Xiong et al., 2011; Huang et al., 2014; Xia et al., 2015). Thus, the materials that contributed to the Permian–Triassic CC growth in the EKOB included those from both slab and subcontinental mantle. Our proposal also emphasizes the role of slab material, a key component in the "continental collision zone model" (Mo et al., 2008; Niu et al., 2013), in the growth of CC. However, the Gouli batholith, which is similar to most of Permian–Triassic granitoids in the EKOB, formed in a subduction setting rather than a continental-collision setting, which is essentially different from the "continental collision zone model". Additionally, we underline the role of subcontinental mantle in the construction of CC in the EKOB. In summary, CC growth can occur in both subduction and syn-collision settings, and the crustal growth in a subduction setting played a more important role within the EKOB because of large amounts of subduction-related magmatic rocks in this area (Fig. 10).

7. Conclusions

(1) The subduction of the A'nyemaqen Ocean terminated at ~237 Ma and the ubiquitous Permian-Triassic granitoids (260–237 Ma) in the EKOB were produced in a subduction setting.

(2) The Gouli batholith intruded during the Middle Triassic (ca. 242 Ma) and originated from the mixing of slab-derived felsic magma and subcontinental mantle-derived mafic magma. The felsic magma end-member was generated from the partial melting of the

subducting oceanic crust and terrigenous sediments, leaving garnet-bearing amphibolite as residue. This magma, which included limited involvement from mafic magma, generated the Xiangride granodiorite after minor fractional crystallization. The mafic magma was produced through the partial melting of subcontinental mantle and generated the Asiha quartz diorite and MMEs through different degrees of mixing with the felsic magma.

(3) The dominant CC growth in the EKOB during the Permian–Triassic occurred in a subduction setting, and both slab and subcontinental mantle contributed to the vertical growth of the CC.

Acknowledgments

We thank the Editor-in-Chief Xian-Hua Li and two anonymous reviewers for their valuable comments, which improved this paper. This research was jointly supported by the Fundamental Research Founds for the Central Universities, China University of Geosciences (Wuhan) (CUGL17043), and the China Geological Survey (12120114081401, 12120114000701). We appreciate the valuable help of Shaoqing Zhao, Zhen Wang and Xiaolong Wang from the CUG during the fieldwork. Thanks are also due to Prof. Yaoling Niu for providing a valuable discussion on the petrogenesis of granitoids and MMEs.

References:

Barbarin, B., 2005. Mafic magmatic enclaves and mafic rocks associated with some granitoids of the central Sierra Nevada batholith, California: nature, origin, and relations with the hosts. Lithos 80, 155-177.

Castillo, P.R., 2012. Adakite petrogenesis. Lithos 134-135, 304-316.

Castillo, P.R., Janney, P.E., Solidum, R.U., 1999. Petrology and geochemistry of Camiguin Island, southern Philippines: insights to the source of adakites and other lavas in a complex arc setting. Contributions to Mineralogy and Petrology 134, 33-51.

Chapman, J.B., Ducea, M.N., DeCelles, P.G., Profeta, L., 2015. Tracking changes in crustal thickness during orogenic evolution with Sr/Y: An example from the North American Cordillera. Geology 43, 919-922.

Charan, S.N., Babu, E.V.S.S., Naqvi, S.M., Prathap, J.G.R., Mohan, M.R., Sarma, D.S., 2009. REE-HFSE distribution/partitioning between garnetiferous restites and TTG from Nademavinapura area, Western Dharwar craton. Journal of the Geological Society of India 73, 371-378.

Chauvel, C., Lewin, E., Carpentier, M., Arndt, N.T., Marini, J., 2008. Role of recycled oceanic basalt and sediment in generating the Hf-Nd mantle array. Nature Geoscience 1, 64-67.

Chen, G.C., Pei, X.Z., Li, R.B., Li, Z.C., Pei, L., Liu, Z.Q., Chen, Y.X., Liu, C.J., Gao, J.M., Wei, F.H., 2013. Zircon U-Pb Geochronology, Geochemical Characteristics and Geological Significance of Cocoe A' Long Quartz Diorites Body from the Hongshuichuan Area in East

Kunlun. Acta Geologica Sinica 87, 178-196 (in Chinese with English abstract).

Chen, L., Sun, Y., Pei, X.Z., Gao, M., Tao, F., Zhang, Z.Q., Chen, W., 2001. Northernmost Paleo-Tethyan oceanic basin in Tibet: geochronological evidence from 40Ar_39Ar age dating of Dur'ngoi ophiolite. Chinese Science Bulletin 46, 1203-1205.

Chen, N.S., Wang, X.Y., Zhang, H.F., Sun, M., Li, X.Y., Chen, Q., 2007a. Geochemistry and Nd-Sr-Pb isotopic compositions of granitoids from Qaidam and Oulongbuluke micro-blocks, NW China: constraints on basement nature and tectonic affinity. Earth Science —Journal of China University of Geosciences 32, 7-21 (in Chinese with English abstract).

Chen, N.S., Xia, X.P., Li, X.Y., Sun, M., Xu, P., Liu, X.M., Wang, X.Y., Wang, Q.Y., 2007b. Timing of magmatism of the gneissic-granite plutons along north Qaidamu margin and implications for Precambrian crustal accretions: zircon U-Pb dating and Hf isotope evidences. Acta Petrologica Sinica 23, 501-512 (in Chinese with English abstract).

Chen, N.S., Sun, M., Wang, Q.Y., Zhao, G.C., Chen, Q., Shu, G.Y., 2007c. EMP chemical ages of monazites from central zone of the Eastern Kunlun Orogen: records of multi-tectonometamorphic events. Chinese Science Bulletin 52, 1297-1306 (in Chinese).

Chen, S., Niu, Y.L., Li, J.Y., Sun, W.L., Zhang, Y., Hu, Y., Shao, F.L., 2016. Syn-collisional adakitic granodiorites formed by fractional crystallization: Insights from their enclosed mafic magmatic enclaves (MMEs) in the Qumushan pluton, North Qilian Orogen at the northern margin of the Tibetan Plateau. Lithos 248-251, 455-468.

Chen, X.H., Gehrels, G., An, Y., Li, L., Jiang, R.B., 2012. Paleozoic and Mesozoic basement

magmatisms of Eastern Qaidam Basin, Northern Qinghai-Tibet Plateau: LA-ICP-MS zircon U-Pb geochronology and its geological significance. Acta Geologica Sinica 86, 350-369.

Chen, X.H., Yin, A., George, G., Li, L., Jiang, R.B., 2011. Chemical geodynamics of granitic magmatism in the basement of the Eastern Qaidam Basin, Northern Qinghai-Tibet Plateau. Acta Geologica Sinica 85, 157-171 (in Chinese with English abstract).

Chen, Y.X., Pei, X.Z., Li, R.B., Li, Z.C., Pei, L., Liu, C.J., Yang, J., 2014. Geochemical characteristics and tectonic significance of meta-sedimentary rocks from Naij Tal group，eastern section of East Kunlun. Geoscience 28, 489-500 (in Chinese with English abstract).

Chiaradia, M., 2015. Crustal thickness control on Sr/Y signatures of recent arc magmas: an Earth scale perspective. Scientific Reports 5, 8115.

Dai, H., Zheng, J., Zhou, X., Griffin, W.L., 2016. Generation of continental adakitic rocks: Crystallization modeling with variable bulk partition coefficients. Lithos 272-273, 222-231.

Dai, J.G., Wang, C.S., Hourigan, J., Santosh, M., 2013. Multi-stage tectono-magmatic events of the Eastern Kunlun Range, northern Tibet: insights from U–Pb geochronology and (U–Th)/He thermochronology. Tectonophysics 599, 97-106.

Defant, M.J., Drummond, M.S., 1990. Derivation of some modern arc magmas by melting of young subducted lithosphere. Nature 347, 662-665.

Didier, J., Barbarin, B., 1991. Enclaves and granite petrology, Developments in Petrology,

13th ed. Elsevier, Amsterdam.

Ding, Q.F., Jiang, S.Y., Sun, F.Y., 2014. Zircon U–Pb geochronology, geochemical and Sr–Nd–Hf isotopic compositions of the Triassic granite and diorite dikes from the Wulonggou mining area in the Eastern Kunlun Orogen, NW China: petrogenesis and tectonic implications. Lithos 205, 266-283.

Ding, S., Huang, H., Niu, Y.N., Zhao, Z.D., Yu, X.H., Mo, X.X., 2011. Geochemistry，geochronology and petrogenesis of East Kunlun high Nb-Ta rhyolites. Acta Petrologica Sinica 27, 3603-3614 (in Chinese with English abstract).

Dorais, M.J., Lira, R., Chen, Y.D., Tingey, D., 1997. Origin of biotite-apatite-rich enclaves, Achala batholith, Argentina. Contributions to Mineralogy and Petrology 130, 31-46.

Drummond, M.S., Defant, M.J., 1990. A model for trondhjemite–tonalite–dacite genesis and crustal growth via slab melting: Archean to modern comparisons. Journal of Geophysical Research 95, 21503-21521.

Feng, C.Y., Wang, X.P., Shu, X.F., Zhang, A.K., Xiao, Y., Liu, J.N., Ma, S.C., Li, G.C., Li, D.X., 2011. Isotopic chronology of the Hutouya skarn lead-zinc polymetallic ore district in Qimantage area of Qinghai province and its geological significance. Journal of Jilin University (Earth Science Edition) 41, 1806-1817 (in Chinese with English abstract).

Fu, L.B., Wei, J.H., Tan, J., Santosh, M., Zhang, D.H., Chen, J.J., Li, Y.J., Zhao, S.Q., Peng, L.N., 2016. Magma mixing in the Kalaqin core complex, northern North China Craton: linking deep lithospheric destruction and shallow extension. Lithos 260, 390-412.

Gao, S., Rudnick, R.L., Yuan, H.L., Liu, X.M., Liu, Y.S., Xu, W.L., Ling, W.L., Ayers, J., Wang, X.C.,

Wang, Q.H., 2004. Recycling lower continental crust in the North China craton. Nature 432, 892-897.

Gao, Y.B., 2013. The intermediate-acid intrusive magmatism and mineralization in Oimantag, East Kunlun Moutains. Doctor. Xi'an, Chang'an University (in Chinese with English abstract).

Gao, Y.B., Li, K., Qian, B., Li, W.Y., Li, D.S., Su, S.S., Zhang, C.G., Zhang, D.M., Wang, S.M., 2015. The genesis of granodiorites and dark enclaves from the Kaerqueka deposit in east Kunlun belt: evidence from zircon U-Pb dating, geochemistry and Sr-Nd-Hf isotopic compositions. Geology in China 42, 646-662 (in Chinese with English abstract).

Gao, Y.B., Li, W.Y., Ma, X.G., Zhang, Z.W., Tang, Q.Y., 2012. Genesis, geochronology and Hf isotopic compositions of the magmatic rocks in Galinge iron deposit, eastern Kunlun. Journal of Lanzhou University (Natural Sciences) 48, 36-47 (in Chinese with English abstract).

Gehrels, G., Kapp, P., DeCelles, P., Pullen, A., Blakey, R., Weislogel, A., Ding, L., Guynn, J., Martin, A., McQuarrie, N., Yin, A., 2011. Detrital zircon geochronology of pre-Tertiary strata in the Tibetan-Himalayan orogen. Tectonics 30, 1-27.

Gradstein, F.M., Ogg, J.G., Schmitz, M.D., Ogg, G.M., 2012. The geologic time scale 2012. Elsevier's Science and Technology Rights Department, Oxford, UK.

Guo, A.L., Zhang, G.W., Sun, Y.G., Cheng, Y.S., Qiang, J., 2007. Sr-Nd-Pb isotopic geochemistry of late-Paleozoic mafic volcanic rocks in the surrounding areas of Gonghe basin, Qinghai Province and geological implications. Acta Petrologica Sinica 23, 747-754

(in Chinese with English abstract).

Harris, N.B.W., Zhang, Y., 1988. Isotope geochemistry of the 1985 Tibet geotraverse, Lhasa to Golmud. Philosophical Transactions of the Royal Society of London 327, 263-285.

He, D.F., Dong, Y.P., Liu, X.M., Yang, Z., Sun, S.S., Cheng, B., Li, W., 2016. Tectono-thermal events in East Kunlun, Northern Tibetan Plateau: evidence from zircon U–Pb geochronology. Gondwana Research 30, 179-190.

Hoffmann, J.E., Münker, C., Polat, A., Rosing, M.T., Schulz, T., 2011. The origin of decoupled Hf–Nd isotope compositions in Eoarchean rocks from southern West Greenland. Geochimica et Cosmochimica Acta 75, 6610-6628.

Holden, P., Halliday, A.N., Stephens, W.E., 1987. Neodymium and strontium isotope content of microdiorite enclaves points to mantle input to granitoid production. Nature 330, 53-56.

Hu, Z.C., Liu, Y.S., Gao, S., Liu, W.G., Zhang, W., Tong, X.R., Lin, L., Zong, K.Q., Li, M., Chen, H.H., Zhou, L., Yang, L., 2012. Improved in situ Hf isotope ratio analysis of zircon using newly designed X skimmer cone and jet sample cone in combination with the addition of nitrogen by laser ablation multiple collector ICP-MS. Journal of Analytical Atomic Spectrometry 27, 1391-1399.

Huang, H., Niu, Y.L., Nowell, G., Zhao, Z.D., Yu, X.H., Zhu, D.C., Mo, X.X., Ding, S., 2014. Geochemical constraints on the petrogenesis of granitoids in the East Kunlun Orogenic belt, northern Tibetan Plateau: implications for continental crust growth through syn-collisional felsic magmatism. Chemical Geology 370, 1-18.

Kepezhinskas, P., Defant, M.J., Drummond, M.S., 1996. Progressive enrichment of island arc mantle by melt-peridotite interaction inferred from Kamchatka xenoliths. Geochimica et Cosmochimica Acta 60, 1217-1229.

Kumar, S., Rino, V., 2006. Mineralogy and geochemistry of microgranular enclaves in Palaeoproterozoic Malanjkhand granitoids, central India: evidence of magma mixing, mingling, and chemical equilibration. Contributions to Mineralogy and Petrology 152, 591-609.

Kumar, S., Rino, V., Pal, A.B., 2004. Field evidence of magma mixing from microgranular enclaves hosted in Palaeoproterozoic Malanjkhand granitoids, Central India. Gondwana Research 7, 539-548.

Li, B.Y., Sun, F.Y., Yu, X.F., Qian, Y., Wang, G., Yang, Y.Q., 2012. U-Pb dating and geochemistry of diorite in the eastern section from eastern Kunlun middle uplifted basement and granitic belt. Acta Petrologica Sinica 28, 1163-1172 (in Chinese with English abstract).

Li, J.C., Jia, Q.Z., Du, W., Su, Y.Z., Kong, H.L., Nan, K.E.W., Yang, B.R., 2014. LA-ICP-MS zircon dating and geochemical characteristics of quartz diorite in Asiha gold deposit in east segment of the Eastern Kunlun. Journal of Jilin University (Earth Science Edition) 44, 1188-1199 (in Chinese with English abstract).

Li, R.B., 2012. Research on the Late Paleozoic-Early Mesozoic orogeny in East Kunlun Orogen. Doctor. Xi'an, Chang'an University (in Chinese with English abstract).

Li, R.B., Pei, X.Z., Li, Z.C., Liu, Z.Q., Chen, G.C., Chen, Y.X., Wei, F.H., Gao, J.M., Liu, C.J., Pei, L.,

2012. Geological characteristics of Late Paleozoic - Mesozoic unconformities and their response to some significant tectonic events in eastern part of Eastern Kunlun. Earth Science Frontier 19, 244-254 (in Chinese with English abstract).

Li, S., Huang, F., Li, H., 2002. Post-collisional lithosphere delamination of the Dabie-Sulu orogen. Chinese Science Bulletin 47, 259-263.

Li, S.J., Sun, F.Y., Feng, C.Y., Liu, Z.H., Zhao, J.W., Li, Y.C., Wang, S., 2008. Geochronological study on Yazigou polymetallic deposit in Eastern Kunlun, Qinhai Province. Acta Geologica Sinica 82, 949-955 (in Chinese with English abstract).

Li, S.M., Zhu, D.C., Wang, Q., Zhao, Z.D., Sui, Q.L., Liu, S.A., Liu, D., Mo, X.X., 2014. Northward subduction of Bangong–Nujiang Tethys: insight from Late Jurassic intrusive rocks from Bangong Tso in western Tibet. Lithos 205, 284-297.

Li, Z.C., Pei, X.Z., Liu, Z.Q., Li, R.B., Pei, L., Chen, G.C., Liu, C.J., Chen, Y.X., Gao, J.M., Wei, F.H., Wu, S.K., Wang, Y.C., Yang, J., 2013. Geochronology and geochemistry of the Gerizhuotuo diorites from the Buqingshan Tectonic Mélange Belt in the southern margin of East Kunlun and their geologic implications. Acta Geologica Sinica 87, 1089-1103 (in Chinese with English abstract).

Liu, C.D., 2008. The granite magma mixing in east of the Eastern Kunlun Orogenic belt. Geological Publishing House, Beijing (in Chinese).

Liu, C.D., Mo, X.X., Luo, Z.H., Yu, X.H., Shen, H.W., Li, S.W., Zhao, X., 2004. Crust-mantle magma mixing in Eastern Kunlun: evidence from zircon SHRIMP dating. Chinese Science Bulletin 49, 596-602 (in Chinese).

Liu, C.D., Zhang, W.Q., Mo, X.X., Luo, Z.H., Yu, X.H., Li, S.W., Zhao, X., 2002. Features and origin of mafic microgranular enclaves in the Yuegelu granite in the Eastern Kunlun. Geological Bulletin of China 21, 739-744 (in Chinese with English abstract).

Liu, J.N., Feng, C.Y., Qi, F., Li, G.C., Ma, S.C., Xiao, Y., 2012. SIMS zircon U-Pb dating and fluid inclusion studies of Xiadeboli Cu-Mo ore district in Dulan County, Qinghai Province, China. Acta Petrologica Sinica 28, 679-690 (in Chinese with English abstract).

Liu, J.P., Lai, J.Q., Gu, X.P., Wang, X.J., Mao, Y., Song, W.B., 2012. Geochemistry and zircon LA-ICPMS U-Pb geochronology of intrusive body in Saishitang copper deposit, Pb geochronology of Qinghai Province, China. The Chinese Journal of Nonferrous Metals 22, 622-632 (in Chinese with English abstract).

Liu, Y.S., Hu, Z.C., Gao, C.G., Gao, S., Günther, D., Xu, J., Gao, C.G., Chen, H.H., 2008a. In situ analysis of major and trace elements of anhydrous minerals by LA-ICP-MS without applying an internal standard. Chemical Geology 257, 34-43.

Liu, Y.S., Zong, K.Q., Kelemen, P., Gao, S., 2008b. Geochemistry and magmatic history of eclogites and ultramafic rocks from the Chinese continental scientific drill hole: Subduction and ultrahigh-pressure metamorphism of lower crustal cumulates. Chemical Geology 247, 133-153.

Liu, Y.S., Hu, Z.C., Zong, K.Q., Gao, C.G., Gao, S., Xu, J., Chen, H.H., 2010. Reappraisement and refinement of zircon U-Pb isotope and trace element analyses by LA-ICP-MS. Chinese Science Bulletin 55, 1535-1546.

Liu, Z.Q., Pei, X.Z., Li, R.B., Li, Z.C., Zhang, X.F., Liu, Z.G., Chen, G.C., Chen, Y.X., Ding, S.P., Guo,

J.F., 2011. LA-ICP-MS zircon U-Pb geochronology of the two suites of ophiolites at the Buqingshan area of the A'nyemaqen Orogenic Belt in the southern margin of East Kunlun and its tectonic implication. Acta Geologica Sinica 85, 185-194 (in Chinese with English abstract).

Ludwig, K.R., 2012. User's manual for Isoplot 3.75——A geochronological toolkit for Microsoft Excel. Berkeley Geochronology Center Special Publication No. 5, Berkeley.

Ma, C.Q., Xiong, F.H., Yin, S., Wang, L.X., Gao, K., 2015. Intensity and cyclicity of orogenic magmatism: An example from a Paleo-Tethyan granitoid batholith，Eastern Kunlun，northern Qinghai-Tibetan Plateau. Acta Petrologica Sinica 31, 3555-3568 (in Chinese with English abstract).

Macpherson, C.G., Dreher, S.T., Thirlwall, M.F., 2006. Adakites without slab melting: high pressure differentiation of island arc magma, Mindanao, the Philippines. Earth and Planetary Science Letters 243, 581-593.

Maniar, P.D., Piccoli, P.M., 1989. Tectonic discrimination of granitoids. Geological Society of America Bulletin 101, 635-643.

Martin, H., 1999. Adakitic magmas: modern analogues of Archaean granitoids. Lithos 46, 411-429.

Mattern, F., Schneider, W., Li, Y., Li, X., 1996. A traverse through the western Kunlun (Xinjiang, China): tentative geodynamic implications for the Paleozoic and Mesozoic. Geologische Rundschau 85, 705-722.

McLeod, C.L., Davidson, J.P., Nowell, G.M., de Silva, S.L., 2012. Disequilibrium melting during

crustal anatexis and implications for modeling open magmatic systems. Geology 40, 435-438.

Meng, F., Zhang, J., Yang, J., 2005. Subducted continental arc: geochemical and isotopic evidence of gneisses in the North Qaidam. Acta Geologica Sinica 79, 46-55 (in Chinese with English abstract).

Middlemost, E.A.K., 1985. Magmas and magmatic rocks: an introduction to igneous petrology. Longman, London.

Middlemost, E.A.K., 1994. Naming materials in the magma/igneous rock system. Earth Science Reviews 37, 215-224.

Mo, X.X., Luo, Z.H., Deng, J.F., Yu, X.H., Liu, C.D., Chen, H.W., Yuan, W.M., Liu, Y.H., 2007. Granitoids and crustal growth in the East-Kunlun Orogenic Belt. Geological Journal of China Universities 13, 403-414 (in Chinese with English abstract).

Mo, X.X., Niu, Y.L., Dong, G.C., Zhao, Z.D., Hou, Z.Q., Zhou, S., Ke, S., 2008. Contribution of syncollisional felsic magmatism to continental crust growth: a case study of the Paleogene Linzizong volcanic succession in southern Tibet. Chemical Geology 250, 49-67.

Moyen, J., 2009. High Sr/Y and La/Yb ratios: the meaning of the “adakitic signature”. Lithos 112, 556-574.

Nandedkar, R.H., Hürlimann, N., Ulmer, P., Müntener, O., 2016. Amphibole–melt trace element partitioning of fractionating calc-alkaline magmas in the lower crust: an experimental study. Contributions to Mineralogy and Petrology 171, 71.

Ni, J.Y., 2010. Zircon U-Pb age and tectonic setting of Permian- Triassic volcanic rock in East Kunlun Orogenic Belt. Master. Beijing, Chinese Academy of Geological Sciences (in Chinese with English abstract).

Niu, Y., O'Hara, M.J., 2009. MORB mantle hosts the missing Eu (Sr, Nb, Ta and Ti) in the continental crust: new perspectives on crustal growth, crust–mantle differentiation and chemical structure of oceanic upper mantle. Lithos 112, 1-17.

Niu, Y.L., Zhao, Z.D., Zhu, D.C., Mo, X.X., 2013. Continental collision zones are primary sites for net continental crust growth — A testable hypothesis. Earth Science Reviews 127, 96-110.

Peccerillo, R., Taylor, S.R., 1976. Geochemistry of Eocene calc-alkaline volcanic rocks from the Kastamonu area, Northern Turkey. Contribution to Mineralogy and Petrology 58, 63-81.

Ramos, F.C., Reid, M.R., 2005. Distinguishing melting of heterogeneous mantle sources from crustal contamination: insights from Sr isotopes at the phenocryst scale, Pisgah Crater, California. Journal of Petrology 46, 999-1012.

Rapp, R.P., Shimizu, N., Norman, M.D., Applegate, G.S., 1999. Reaction between slab-derived melts and peridotite in the mantle wedge: experimental constraints at 3.8 GPa. Chemical Geology 160, 335-356.

Roger, F., Arnaud, N., Gilder, S., Tapponnier, P., Jolivet, M., Brunel, M., Malavieille, J., Xu, Z., Yang, J., 2003. Geochronological and geochemical constraints on Mesozoic suturing in east central Tibet. Tectonics 22, 1-20.

Rudnick, R.L., Gao, S., 2003. Composition of the Continental Crust. In: Holland, H.D., Turekian, K.K. (Eds.), Treatise on Geochemistry 3. Elsevier-Pergamon, Oxford, pp. 1–64.

Sacks, P.E., Secor, D.T., 1990. Delamination in collisional orogens. Geology 18, 999-1002.

Shao, F.L., Niu, Y.L., Liu, Y., Chen, S., Kong, J.J., Duan, M., 2017. Petrogenesis of Triassic granitoids in the East Kunlun Orogenic Belt, northern Tibetan Plateau and their tectonic implications. Lithos 282-283, 33-34.

Shi, C., Li, R.S., Li, S.P., Yu, F.S., Wang, C., Pan, S.J., Zhang, H.D., 2013. Determination of the age for Xingshu valley gold mineralization spots in the eastern segment of Kunlun Orogenic belt and the geochemical characteristics of its surrounding rocks. Chinese Journal of Geology 48, 984-996 (in Chinese with English abstract).

Shimoda, G., Tatsumi, Y., Nohda, S., Ishizaka, K., Jahn, B.M., 1998. Setouchi high-Mg andesites revisited: geochemical evidence for melting of subducting sediments. Earth and Planetary Science Letters 160, 479-492.

Shirey, S.B., Hanson, G.N., 1984. Mantle-derived Archaean monozodiorites and trachyandesites. Nature 310, 222-224.

Song, Z.B., Zhang, Y.L., Chen, X.D., Jiang, L., Li, D.S., Shu, X.F., Su, Y.Z., Li, J.C., Kong, H.L., 2013. Geochemical characteristics of Harizha granite diorite-porphyry in East Kunlun and their geological implications. Mineral Deposits 32, 157-168 (in Chinese with English abstract).

Stern, C.R., Kilian, R., 1996. Role of the subducted slab, mantle wedge and continental crust in the generation of adakites from the Andean Austral Volcanic Zone. Contributions to

Mineralogy and Petrology 123, 263-281.

Sun, S.S., McDonough, W.F., 1989. Chemical and isotopic systematics of oceanic basalts: implications for mantle composition and processes. Geological Society, London, Special Publications 42, 313-345.

Sun, Y., Pei, X.Z., Ding, S.P., Li, R.B., Feng, J.Y., Zhang, Y.F., Li, Z.C., Chen, Y.X., Zhang, X.F., Chen, G.C., 2009. Halagatu Magma Mixing Granite in the East Kunlun Mountains——Evidence from Zircon U-Pb Dating. Acta Geologica Sinica 83, 1000-1010 (in Chinese with English abstract).

Tatsumi, Y., 2006. High-Mg andesites in the Setouchi Volcanic Belt, Southwestern Japan: analogy to Archean magmatism and continental crust formation? Annual Review of Earth and Planetary Sciences 34, 467-499.

Taylor, S.R., 1967. The origin and growth of continents. Tectonophysics 4, 17-34.

Taylor, S.R., 1977. Island arc models and the composition of the continental crust. In: Talwani, M., Pitman, W.C., (Eds.), Island Arcs, Deep Sea Trenches and Back-Arc Basins. American Geophysical Union, Washington, DC, pp. 325–335.

Vernon, R.H., 1984. Microgranitoid enclaves in granites—globules of hybrid magma quenched in a plutonic environment. Nature 309, 438-439.

Vervoort, J.D., Plank, T., Prytulak, J., 2011. The Hf–Nd isotopic composition of marine sediments. Geochimica et Cosmochimica Acta 75, 5903-5926.

Wang, G., Sun, F.Y., Li, B.Y., Li, S.J., Zhao, J.W., Yang, Q.A., 2014. Zircon U-Pb geochronology and geochemistry of diorite in Xiarihamu ore district from East Kunlun and its geological

significance. Journal of Jilin University (Earth Science Edition) 44, 876-891 (in Chinese with English abstract).

Wang, G.C., Xiang, S.Y., Wang, A., John, I.G., Robert, P.W., Zhang, K.X., 2007. Thermochronological constraint to the processes of the East Kunlun and adjacent areas in Mesozoic - Early Cenozoic. Earth Science — Journal of China University of Geosciences 32, 605-614 (in Chinese with English abstract).

Wang, Q., McDermott, F., Xu, J., Bellon, H., Zhu, Y., 2005. Cenozoic K-rich adakitic volcanic rocks in the Hohxil area, northern Tibet: lower-crustal melting in an intracontinental setting. Geology 33, 465.

Wang, S., Feng, C.Y., Li, S.J., Jiang, J.H., Li, D.S., Su, S.S., 2009. Zircon SHRIMP U-Pb dating of granodiorite in the Kaerqueka polymetallic ore deposit, Qimantage Mountain, Qinghai Province, and its geological implications. Geology in China 36, 74-84 (in Chinese with English abstract).

Wang, X.L., 2012. Studies on geological characteristics and forming age of Southern Xianjia Mountain granitic pluton at east section of East Kunlun Orogenic Belt. Master. Xi' an, Chang' an University (in Chinese with English abstract).

Wu, F.Y., Jahn, B., Wilde, S., Sun, D.Y., 2000. Phanerozoic crustal growth: U–Pb and Sr–Nd isotopic evidence from the granites in northeastern China. Tectonophysics 328, 89-113.

Xi, R.G., Xiao, P.X., Wu, Y.Z., Dong, Z.C., Guo, L., Gao, X.F., 2010. The geological significances, composition and age of the monzonitic granite in Kendekeke iron mine. Northwestern Geology 43 195-202 (in Chinese with English abstract).

Xia, R., Qing, M., Wang, C.M., Li, W.L., 2014. The genesis of the ore-bearing porphyry of the Tuoketuo porphyry Cu-Au (Mo) deposit in the East Kunlun, Qinghai Province: constraints from zircon U-Pb geochronological and geochemistry. Journal of Jilin University (Earth Science Edition) 44, 1502-1524 (in Chinese with English abstract).

Xia, R., Wang, C.M., Qing, M., Deng, J., Carranza, E.J.M., Li, W.L., Guo, X.D., Ge, L.S., Yu, W.Q., 2015a. Molybdenite Re-Os, zircon U-Pb dating and Hf isotopic analysis of the Shuangqing Fe-Pb-Zn-Cu skarn deposit, East Kunlun Mountains, Qinghai Province, China. Ore Geology Reviews 66, 114-131.

Xia, R., Wang, C.M., Qing, M., Li, W.L., Carranza, E.J.M., Guo, X.D., Ge, L.S., Zeng, G.Z., 2015b. Zircon U-Pb dating, geochemistry and Sr-Nd-Pb-Hf-O isotopes for the Nan'getan granodiorites and mafic microgranular enclaves in the East Kunlun Orogen: record of closure of the Paleo-Tethys. Lithos 234, 47-60.

Xiao, Y., Feng, C.Y., Liu, J.N., Yu, M., Zhou, J.H., Li, D.X., Zhao, Y.M., 2013. LA-MC-ICP-MS zircon U-Pb dating and sulfur isotope characteristics of Kendekeke Fe-polymetallic deposit, Qinghai Province. Mineral Deposits 32, 177-186 (in Chinese with English abstract).

Xiong, F.H., 2014. Spatial-temporal pattern, petrogenesis and geological implications of Paleo-Tethyan granitoids in the East Kunlun Orogenic belt (eastern segment). Doctor. Wuhan, China University of Geosciences (in Chinese with English abstract).

Xiong, F.H., Ma, C.Q., Jiang, H.A., Liu, B., Zhang, J.Y., Zhou, Q., 2013. Petrogenetic and tectonic significance of Permian calc-alkaline lamprophyres, East Kunlun orogenic belt,

Northern Qinghai-Tibet Plateau. International Geology Review 55, 1817-1834.

Xiong, F.H., Ma, C.Q., Zhang, J.Y., Liu, B., 2011a. LA-ICP-MS zircon U-Pb dating，elements and Sr-Nd-Hf isotope geochemistry of the Early Mesozoic mafic dyke swarms in East Kunlun Orogenic belt. Acta Petrologica Sinica 27, 3350-3364 (in Chinese with English abstract).

Xiong, F.H., Ma, C.Q., Zhang, J.Y., Liu, B., Jiang, H.A., Huang, J., 2011b. Zircon LA-ICP-MS U-Pb dating of Bairiqili gabbro pluton in East Kunlun Orogenic belt and its geological significance. Geological Bulletin of China 30, 1196-1202 (in Chinese with English abstract).

Xiong, F.H., Ma, C.Q., Zhang, J.Y., Liu, B., 2012. The origin of mafic microgranular enclaves and their host granodiorites from East Kunlun, Northern Qinghai-Tibet Plateau: implications for magma mixing during subduction of Paleo-Tethyan lithosphere. Mineralogy and Petrology 104, 211-224.

Xiong, F.H., Ma, C.Q., Zhang, J.Y., Liu, B., Jiang, H.A., 2014. Reworking of old continental lithosphere: an important crustal evolution mechanism in orogenic belts, as evidenced by Triassic I-type granitoids in the East Kunlun orogen, Northern Tibetan Plateau. Journal of the Geological Society 171, 847-863.

Xu, Q.L., Sun, F.Y., Li, B.Y., Qian, Y., Li, L., Yang, Y.Q., 2014. Geochronological dating, geochemical characteristics and tectonic setting of the granite-porphyry in the Mohexiala silver polymetallic deposit, Eastern Kunlun Orogenic Belt. Geotectonica et Metallogenia 38, 421-433 (in Chinese with English abstract).

Xu, W., Zhang, H., Luo, B., Guo, L., Yang, H., 2015. Adakite-like geochemical signature

produced by amphibole-dominated fractionation of arc magmas: An example from the Late Cretaceous magmatism in Gangdese belt, south Tibet. Lithos 232, 197-210.

Yang, J.S., Robinson, P.T., Jiang, C.F., Xu, Z.Q., 1996. Ophiolites of the Kunlun Mountains, China and their tectonic implications. Tectonophysics 258, 215-231.

Yang, Y.Q., Li, B.Y., Xu, Q.L., Zhang, B.S., 2013. Zircon U-Pb ages and its geological significance of the monzonitic granite in the Aikengdelesite, Eastern Kunlun. Northwestern Geology 46, 56-62 (in Chinese with English abstract).

Yin, L.J., Liu, H.J., Yang, L.G., Liu, W.M., 2013. Geochronology, geochemistry and geological significance of granites from the Baishiya skarn iron-polymetallic deposit, Dulan, Qinghai Province. Xinjiang Geology 31, 248-255 (in Chinese with English abstract).

Zhang, G., 2012. Research on geological characteristics, ages and geological significance of the Halagatu granitic rocks in east segment of the East Kunlun Orogen. Master. Xi'an, Chang'an University (in Chinese with English abstract).

Zhang, J.Y., Ma, C.Q., Xiong, F.H., Liu, B., 2012. Petrogenesis and tectonic significance of the Late Permian–Middle Triassic calc-alkaline granites in the Balong region, eastern Kunlun Orogen, China. Geological Magazine 149, 892-908.

Zhao, L., Guo, F., Fan, W.M., Li, C.W., Qin, X.F., Li, H.X., 2012. Origin of the granulite enclaves in Indo-Sinian peraluminous granites, South China and its implication for crustal anatexis. Lithos 150, 209-226.

Zhao, Z.X., Wei, J.H., Fu, L.B., Liang, S.N., Zhao, S.Q., 2017. The Early Paleozoic Xitieshan syn-collisional granite in the North Qaidam ultrahigh-pressure metamorphic belt, NW

China: Petrogenesis and implications for continental crust growth. Lithos 278, 140-152.

Figure captions

Fig. 1. Simplified geology of (A) the Qinghai-Tibetan Plateau which shows the dominant blocks/terrains (after Xia et al., 2015b); (B) the EKOB, which shows the localities of the dated Late Permian-Triassic magmatic rocks (after Xia et al., 2015a); and (C) the study area located at the eastern end of the EKOB, in which the sample locations are illustrated. The ages of the magmatic rocks were all achieved using the zircon U-Pb LA-ICP-MS/ SHRIMP techniques. The references are as follows: (1) (Liu et al., 2011); (2) (Yang et al., 2013); (3) (Xiong et al., 2014); (4) (Xiong et al., 2012); (5) (Xiong, 2014); (6) (He, a thesis submitted to the China University of Geosciences); (7) (Liu et al., 2004); (8) (Zhang, 2012); (9) (Sun et al., 2009); (10) (Xiong et al., 2013); (11) (Dai et al., 2013); (12) (Xiong et al., 2011b); (13) (Liu et al., 2012); (14) (Zhang et al., 2012); (15) (Chen et al., 2012); (16) (Wang et al., 2009); (17) (Song et al., 2013); (18) (Feng et al., 2011) (19) (Gao et al., 2015); (20) (Gao et al., 2012); (21) (Xia et al., 2014); (22) (Xiao et al., 2013); (23) (Liu et al., 2012); (24) (Xu et al., 2014); (25) (Chen et al., 2013); (26) (Yin et al., 2013); (27) (Ding et al., 2014). The ages in (C) are from Xiong (2014) and Zhao et al. (in press).

Fig. 2. Summarized Carboniferous–Jurassic stratigraphic column for the EKOB.

Fig. 3. Representative photographs of (A–B) Xiangride granodiorite and MMEs, (C) MMEs with quartz xenocrysts from the Xiangride granodiorite, (D) the zonal texture of plagioclase

from the Xiangride granodiorite, (E–F) microscopic margins between the Xiangride granodiorite and MMEs, (G) major minerals from the MMEs, (H) a plagioclase xenocryst from the MMEs that enwraps amphiboles and displays growth zonings, (I) acicular apatite from the MMEs, (J) the Asiha quartz diorite with abundant enclaves, and (K–L) major minerals from the Asiha quartz diorite. Abbreviations: Hb–hornblende, Bi–biotite, Pl–plagioclase, Kf–K-feldspar, Ap–apatite, Qz–quartz.

Fig. 4. Zircon CL images and U–Pb concordia plots of the Xiangride granodiorite (A, C) and Asiha quartz diorite (B, D). The selected $^{206}Pb/^{238}U$ ages (white solid circles) and $\varepsilon_{Hf}(t)$ values (yellow dashed circles) are also shown for the corresponding sites. MSWD: mean square of the weighted deviation.

Fig. 5. Chondrite-normalized REE patterns for zircons from (A) sample 1009-1 from the Xiangride granodiorite and (B) sample B1001-1 from the Asiha quartz diorite. The chondrite-normalization values are from Sun and McDonough (1989).

Fig. 6. Plots of (A) Na_2O+K_2O versus SiO_2 (Middlemost, 1994), (B) K_2O versus SiO_2 (Peccerillo and Taylor, 1976; Middlemost, 1985), (C) Na_2O+K_2O-CaO versus SiO_2 (Frost, 2001), and (D) A/NK [molar ratio $Al_2O_3/(Na_2O+K_2O)$] versus A/CNK [molar ratio $Al_2O_3/(CaO+ Na_2O+K_2O)$] (Maniar and Piccoli, 1989) for the Xiangride granodiorite, MMEs, Asiha quartz diorite and Annage hornblende gabbro. The data for the Annage intrusion is from Zhao et al. (in press).

Fig. 7. Selected major element Harker plots for the Xiangride granodiorite, MME, Asiha quartz diorite and Annage hornblende gabbro. The data sources are the same as those in Fig.5.

Fig. 8. Primitive mantle normalized spider diagrams and chondrite-normalized REE patterns for the Xiangride granodiorite (A–B), MMEs (C–D) and Asiha quartz diorite (E–F). The primitive mantle and chondrite-normalized values are from Sun and McDonough (1989). The data sources are the same as those in Fig. 5.

Fig. 9. Plots of (A) $\varepsilon_{Nd}(t)$ versus $(^{87}Sr/^{86}Sr)_i$ and (B) $\varepsilon_{Hf}(t)$ versus T(Ma). The black curves with blue circles in (A) and (C) refer to the mixing trend between the mantle-derived and average/ancient subduction sediment-derived melts with 5 % increments. The parameters for the mantle end-member melt are the reference values of A'nyemaqen MORB (Sr = 225 ppm, Nd = 23 ppm, Hf = 2.4 ppm, $^{87}Sr/^{86}Sr$ = 0.7066913, $^{143}Nd/^{144}Nd$ = 0.51299056; Guo et al., 2007). The Hf isotope value for MORB is inferred from the Nd isotope value following the equation εHf = 1.59εNd + 1.28 by Chauvel et al. (2008). The end-member of the subduction sediments (Shaliuhe granitic gneiss) are after Harris and Zhang (1988) and Chen et al. (2007a, 2007b) (Sr = 300 ppm, Nd = 33 ppm, Hf=4 ppm, $^{87}Sr/^{86}Sr$ = 0.718, $^{143}Nd/^{144}Nd$ = 0.512, $^{176}Hf/^{177}Hf$=0.28218). The data for the Annage intrusion, Bairiqili mafic rocks, lamprophyres, Wulongou diorite, Dulan granitoid host

rocks and enclaves, and Shaliuhe gneiss are from Zhao et al. (in press), Xiong (2014), Xiong et al. (2013), Ding et al. (2014), Huang et al. (2014) and Chen et al. (2007), respectively. The terrestrial array is from Vervoort et al. (2011). All the initial isotopic ratios are calculated at 242 Ma. EM: enriched mantle.

Fig. 10. Temporal distribution of magmatic rocks and sedimentary facies in the EKOB and their relationships with major tectonic events during the Late Paleozoic and Mesozoic; a statistical histogram of the ages of these magmatic rocks is also shown. The numerical and stage time scales are from Gradstein et al. (2012). The timing of the Late-Triassic unconformity is after R.B. Li et al. (2012) and an unpublished geological report. The numbers on the data points refer to the following sources: 1–27 are the same as in Fig.1; (28) (Chen et al., 2001); (29) (Ding et al., 2011); (30) (B.Y. Li et al., 2012); (31) (J.C. Li et al., 2014); (32) (Li et al., 2013); (33) (Wang et al., 2014); (34) (Huang et al., 2014); (35) (Xia et al., 2015b); (36) (Xiong et al., 2014); (37) (Gao, 2013); (38) (Shi et al., 2013); (39) (Wang, 2012); (40) (Zhao et al. in press); (41) (Ni, 2010).

Fig. 11. Plots of Sr/Yb, $(La/Yb)_N$, Sr, and Y versus. SiO_2. The La and Yb contents of chondrite that were used to calculate $(La/Yb)_N$ are from Sun and McDonough (1989).

Fig. 12. Plots of (A) Sr/Y versus Y, (B) $(La/Yb)_N$ versus Yb_N, (C) Mg# versus SiO_2 and (D) Rb versus Y+Nb. The fields for adakite and classical island-arc magmatic rocks in (A–B) are from Martin (1999) and Drummond and Defant (1990). The partial melting curves in (A–B)

for basalt with residues of eclogite, garnet amphibolite and amphibolite are from Drummond and Defant (1990). The mantle/crustal AFC curves in (C) are after Stern and Kilian (1996) (curves 1 and 3) and Rapp et al. (1999) (curve 2). The starting points of curves 1 and 2 in (C) represent a pure slab-melt composition (Stern and Kilian, 1996) and metabasaltic or eclogite experimental melt that is not hybridized with peridotite (Rapp et al., 1999), respectively. The field of metabasaltic and eclogite melts (1–4.0 GPa) is after Stern and Kilian (1996). The fields of metabasaltic and eclogite experimental melts that are hybridized with peridotite are after Rapp et al. (1999). The chondrite-normalized values are from Sun and McDonough (1989). Syn-COLG: syn-collisional granites; WPG: within-plate granites; ORG: oceanic ridge granites; VAG: volcanic arc granites. The data for the Annage intrusion are from Zhao et al. (in press).

Fig. 13. Rock-forming tectonic setting (A) and schematic genetic model for the Gouli batholith (B). The mafic magma, hybrid magma and felsic magma in (B) represent the primitive magma of the hornblende gabbro, quartz diorite and granodiorite from the Gouli batholith, respectively.

Figure 1

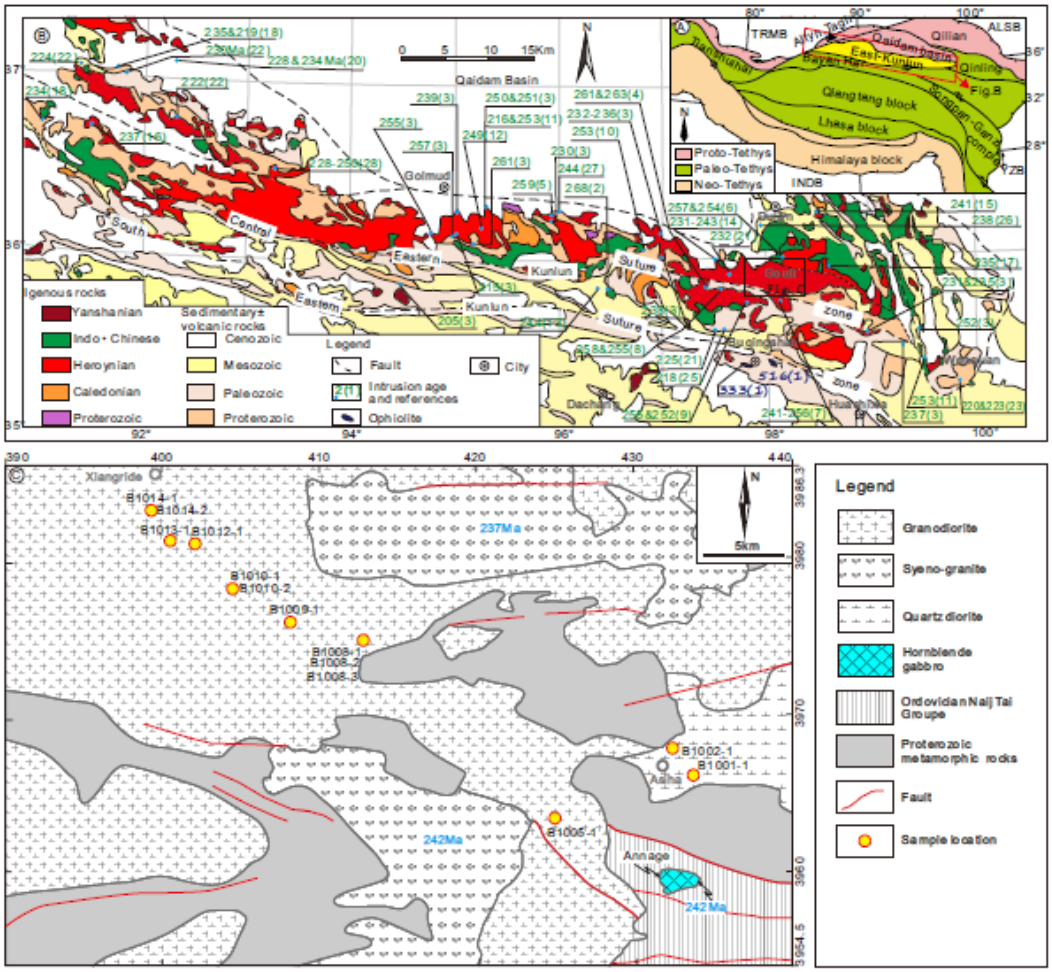

Figure 2

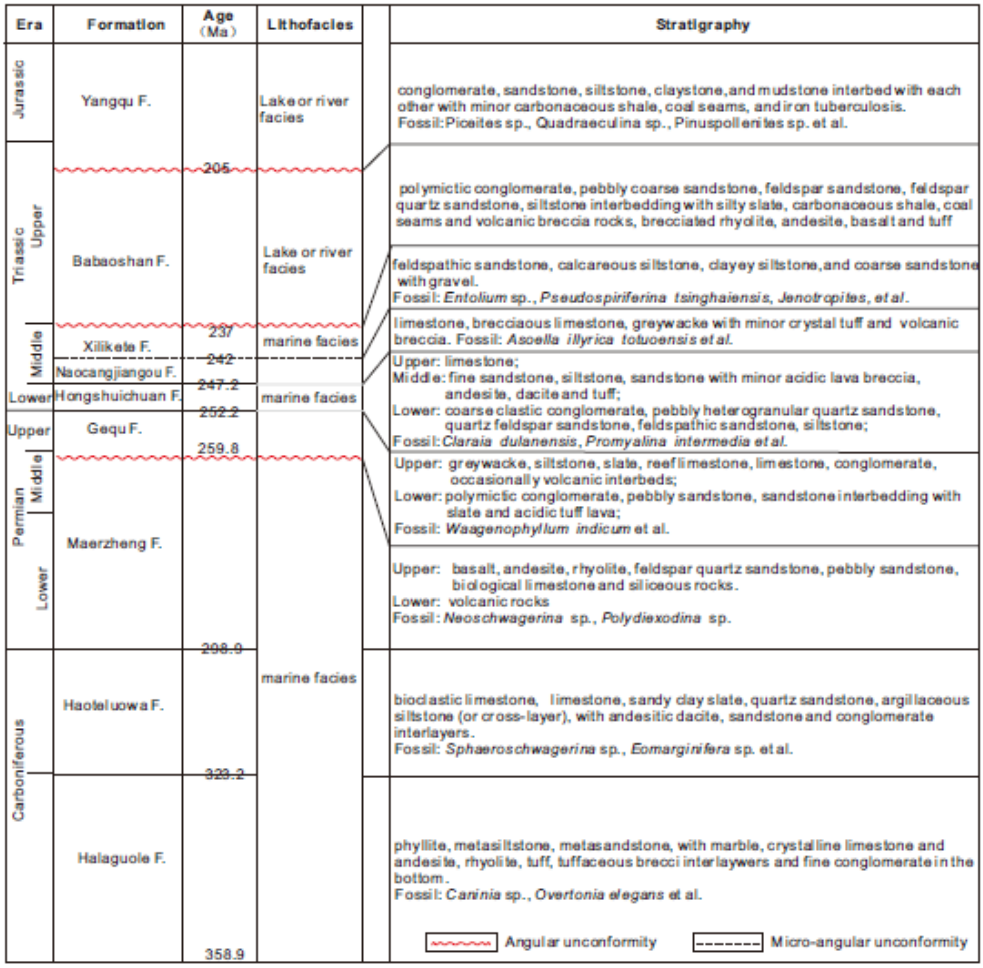

Figure 3

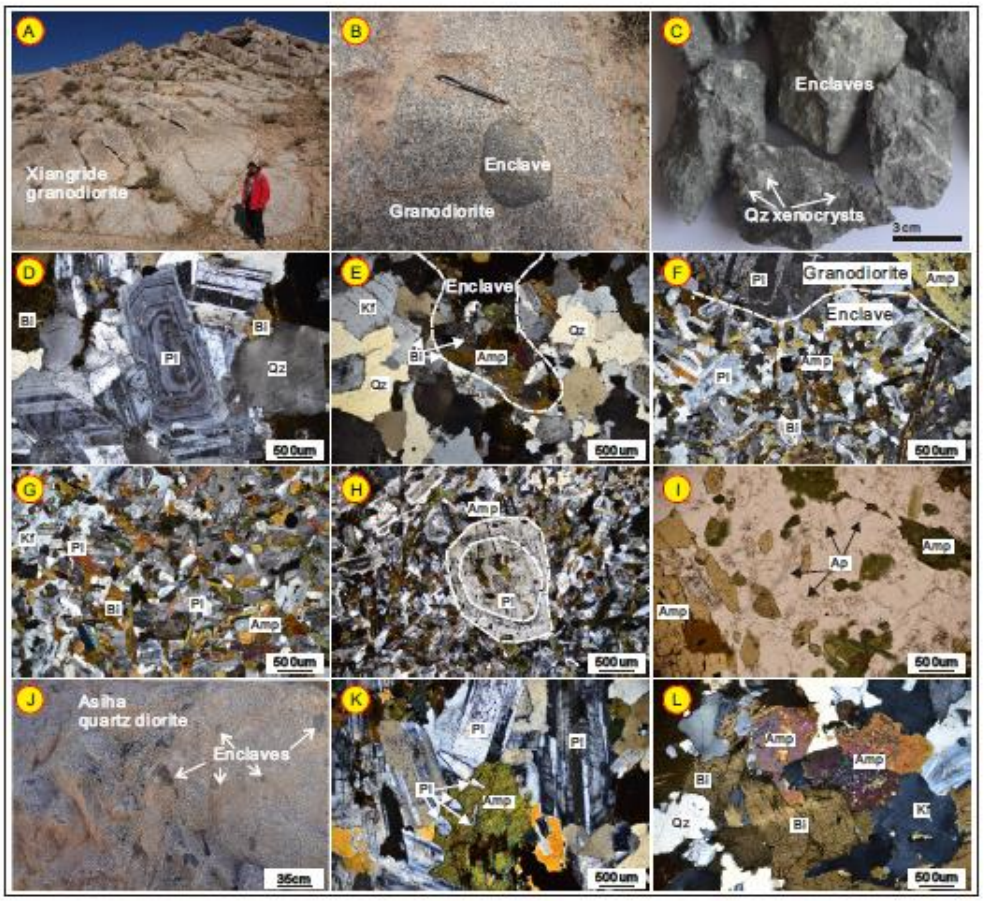

Figure 4

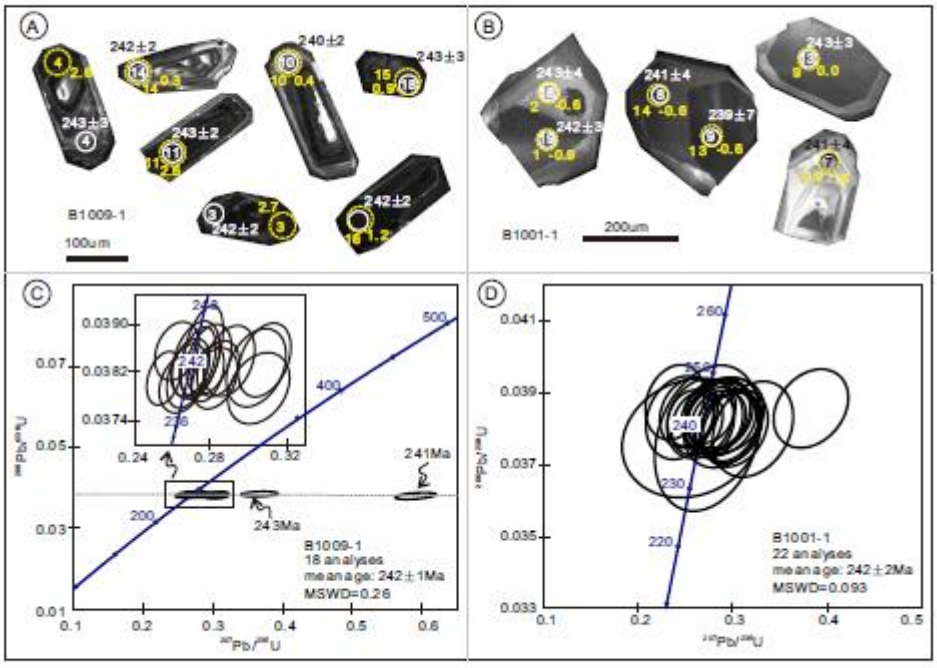

Figure 5

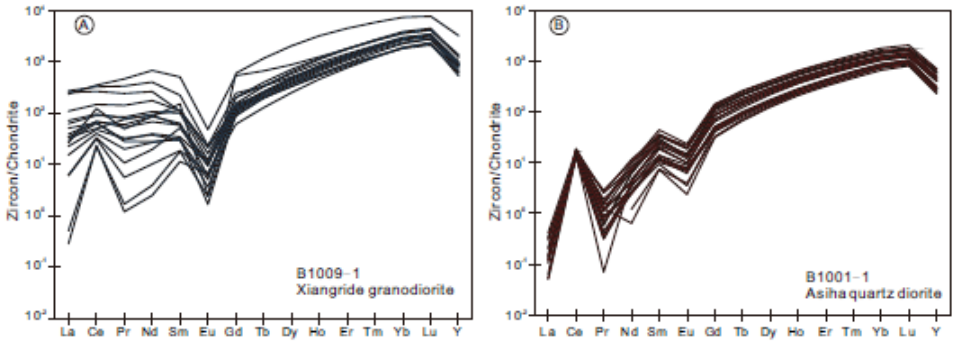

Figure 6

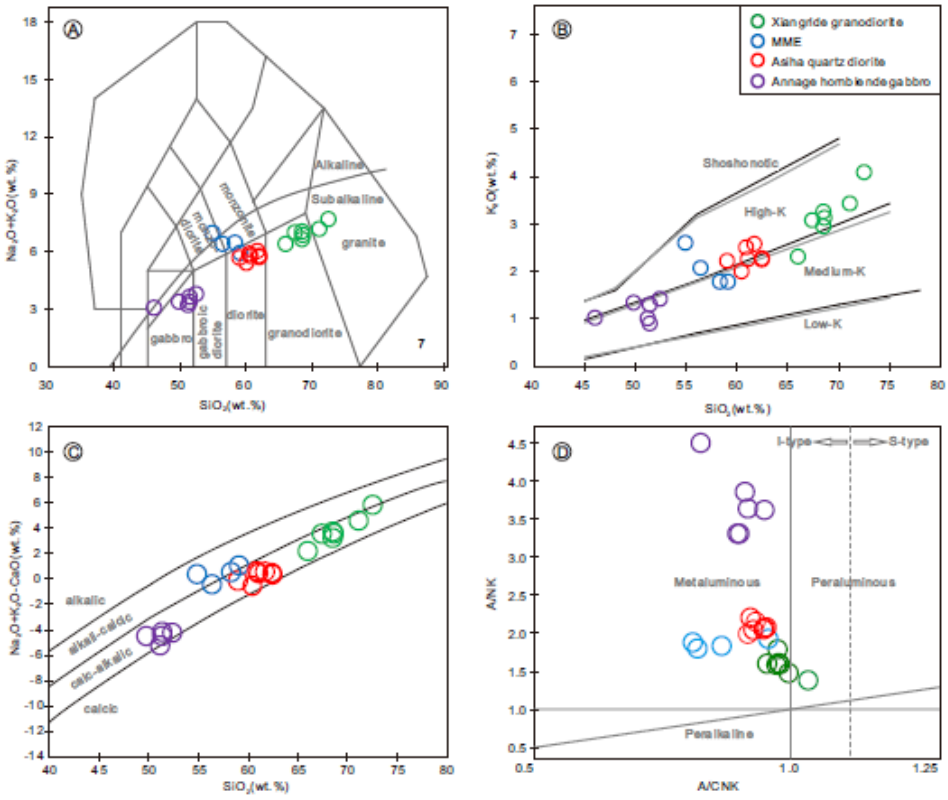

Figure 7

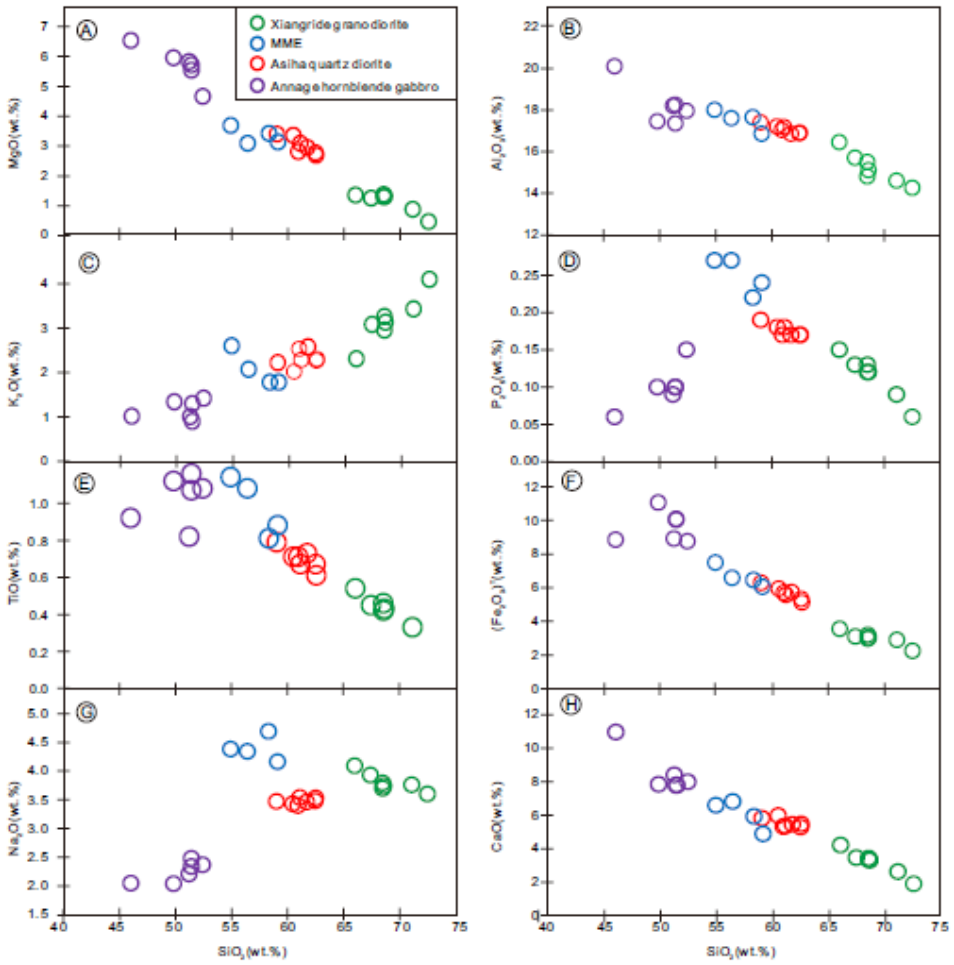

Figure 8

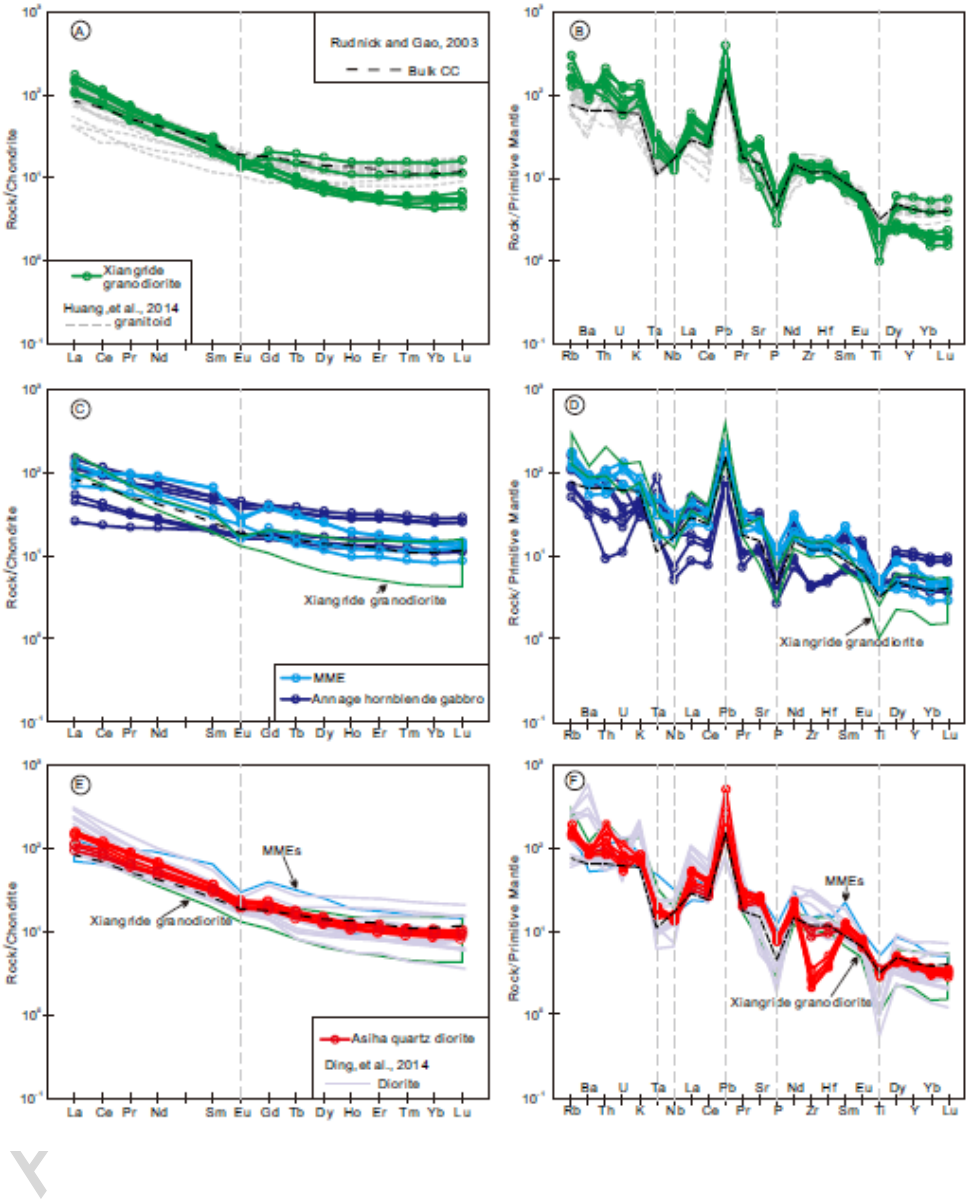

Figure 9

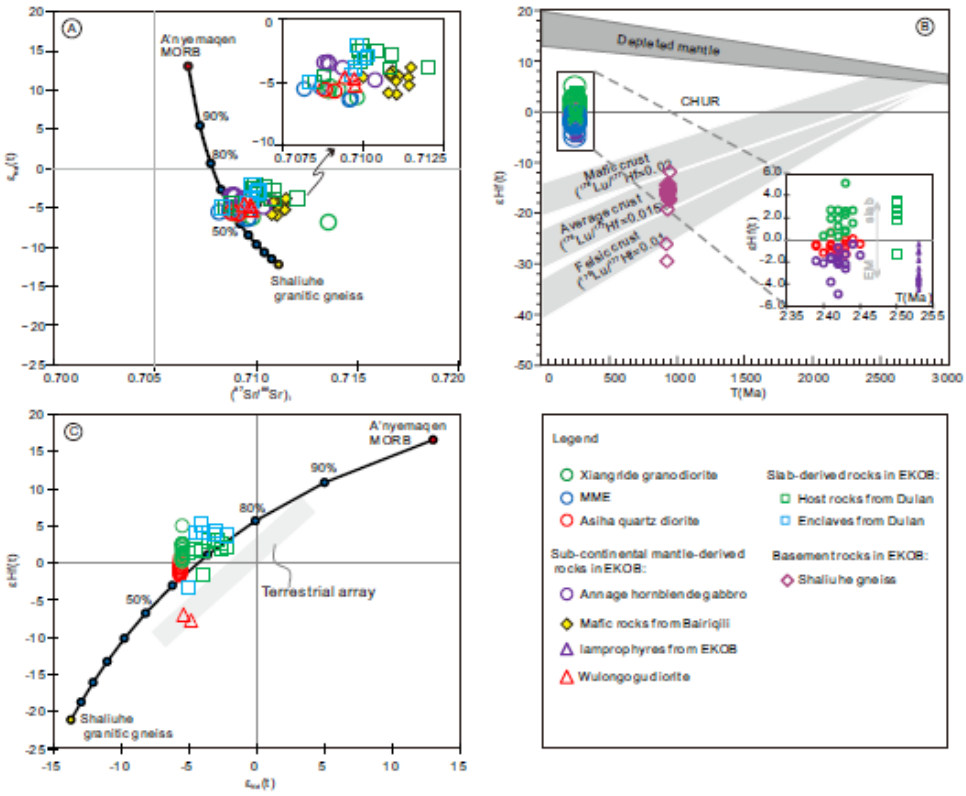

Figure 10

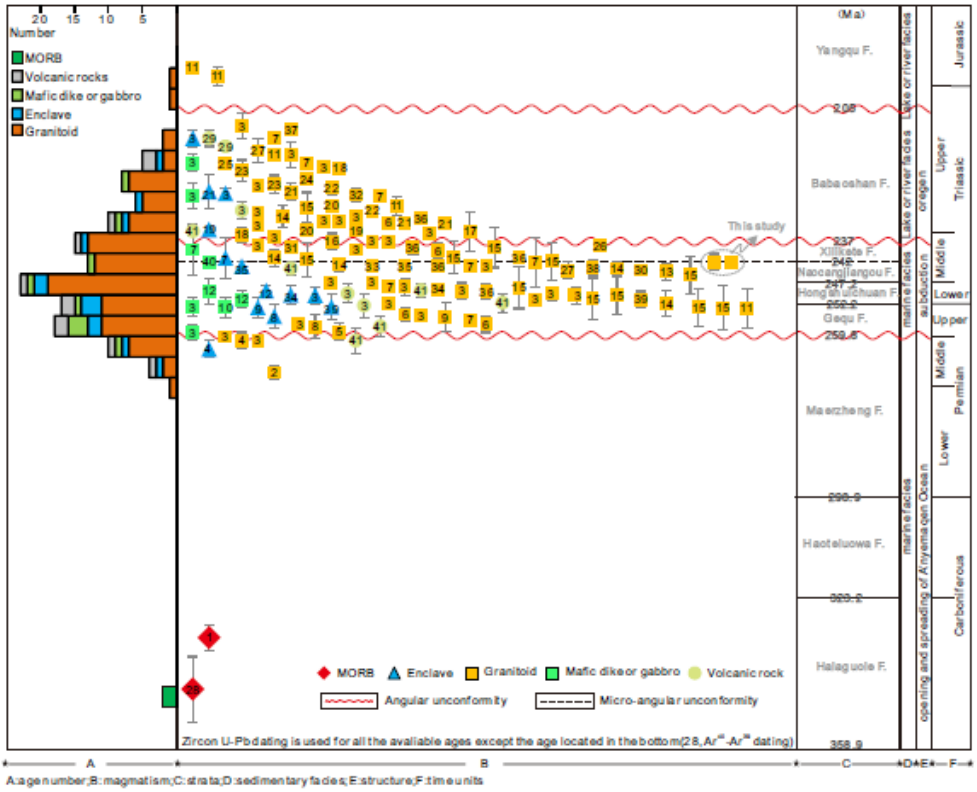

Figure 11

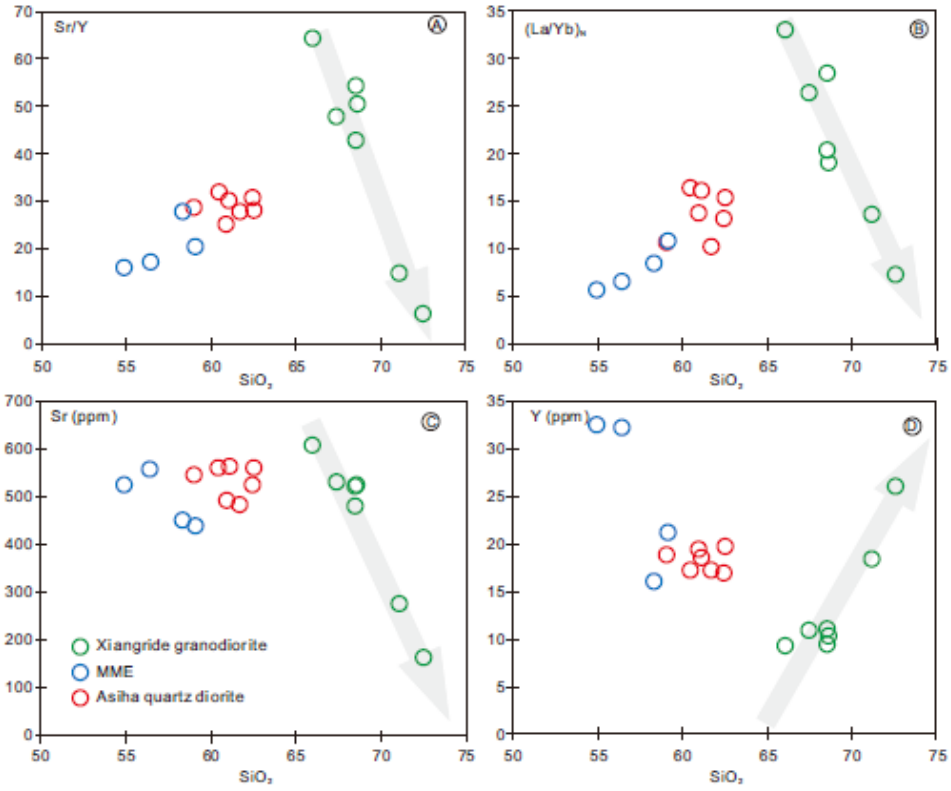

Figure 12

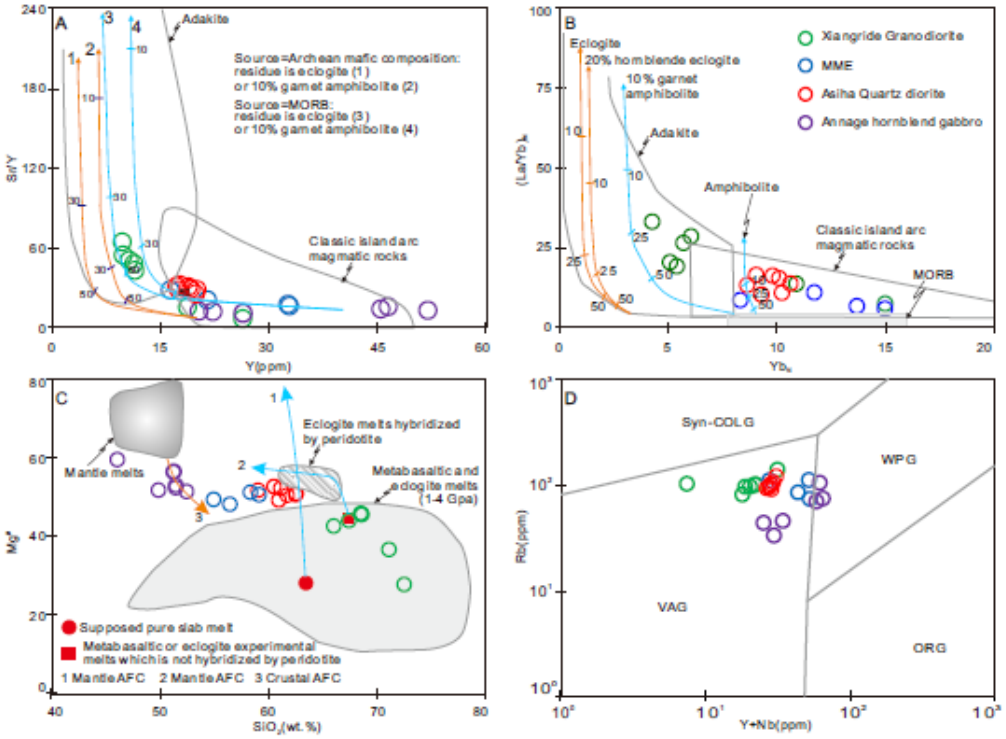

Figure 13

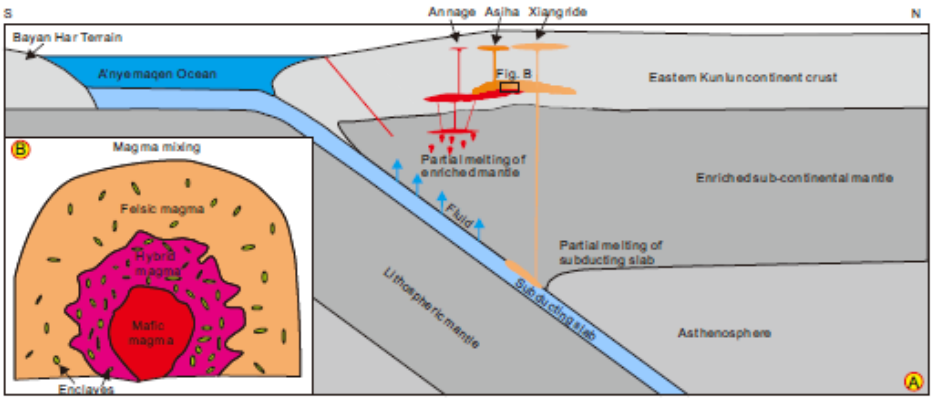

Highlights

(1) The subduction of A'nyemaqen Ocean terminated at ~237 Ma.

(2) The Gouli batholith (ca. 242 Ma) formed by mixing of slab-derived magma and subcontinental mantle-derived magma.

(3) The Permian–Triassic continental crustal growth in the EKOB occurred at subduction setting and both slab and subcontinental mantle contributed to this process.